Journal of Biomolecular NMR (2024) 78:39–60
https://doi.org/10.1007/s10858-023-00431-6

ARTICLE

Beyond slow two-state protein conformational exchange using CEST: applications to three-state protein interconversion on the millisecond timescale

Ved Prakash Tiwari[1] · Debajyoti De[1] · Nemika Thapliyal[1] · Lewis E. Kay[2,3,4] · Pramodh Vallurupalli[1]

Received: 30 August 2023 / Accepted: 15 November 2023 / Published online: 3 January 2024

Abstract

Although NMR spectroscopy is routinely used to study the conformational dynamics of biomolecules, robust analyses of the data are challenged in cases where exchange is more complex than two-state, such as when a 'visible' major conformer exchanges with two 'invisible' minor states on the millisecond timescale. It is becoming increasingly clear that chemical exchange saturation transfer (CEST) NMR experiments that were initially developed to study systems undergoing slow interconversion are also sensitive to intermediate—fast timescale biomolecular conformational exchange. Here we investigate the utility of the amide ^{15}N CEST experiment to characterise protein three-state exchange occurring on the millisecond timescale by studying the interconversion between the folded (F) state of the FF domain from human HYPA/FBP11 (WT FF) and two of its folding intermediates I1 and I2. Although ^{15}N CPMG experiments are consistent with the F state interconverting with a single minor state on the millisecond timescale, ^{15}N CEST data clearly establish an exchange process between F and a pair of minor states. A unique three-state exchange model cannot be obtained by analysis of ^{15}N CEST data recorded at a single temperature. However, including the relative sign of the difference in the chemical shifts of the two minor states based on a simple two-state analysis of CEST data recorded at multiple temperatures, results in a robust three-state model in which the F, I1 and I2 states interconvert with each other on the millisecond timescale ($k_{ex,FI1}$ ~ 550 s^{-1}, $k_{ex,FI2}$ ~ 1200 s^{-1}, $k_{ex,I1I2}$ ~ 5000 s^{-1}), with I1 and I2 sparsely populated at ~ 0.15% and ~ 0.35%, respectively, at 15 °C. A computationally demanding grid-search of exchange parameter space is not required to extract the best-fit exchange parameters from the CEST data. The utility of the CEST experiment, thus, extends well beyond studies of conformers in slow exchange on the NMR chemical shift timescale, to include systems with interconversion rates on the order of thousands/second.

Keywords Protein folding · Conformational exchange · Chemical exchange · CEST · CPMG · FF domain · Folding intermediates

Introduction

Protein molecules are not confined to a single static structure but exchange between different conformations over a range of time-scales (Bahar et al. 2017; Frauenfelder et al. 1991). These different conformational states have important roles in protein function, folding, misfolding, aggregation and disease (Bahar et al. 2017; Karplus and Kuriyan 2005; Sekhar and Kay 2019). Notably, in many cases interconversion occurs between a major conformational state (so called visible state) and one or more sparsely populated states that cannot be detected using traditional NMR techniques (invisible states). Over the past several decades a number of different NMR-based approaches have been developed, including $R_{1,\rho}$ (Deverell et al. 1970), Carr–Purcell–Meiboom–Gill (CPMG)

✉ Lewis E. Kay
kay@pound.med.utoronto.ca

✉ Pramodh Vallurupalli
pramodh@tifrh.res.in

[1] Tata Institute of Fundamental Research Hyderabad, 36/P, Gopanpally Village, Serilingampally Mandal, Ranga Reddy District, Hyderabad 500046, India

[2] Department of Molecular Genetics, University of Toronto, Toronto M5S 1A8, Canada

[3] Department of Chemistry, University of Toronto, Toronto, ON M5S 3H6, Canada

[4] Department of Biochemistry, University of Toronto, Toronto, ON M5S 1A8, Canada

relaxation dispersion (Carr and Purcell 1954; Meiboom and Gill 1958), Dark state exchange saturation transfer (DEST) (Fawzi et al. 2010, 2011) and chemical exchange saturation transfer (CEST) techniques (Forsen and Hoffman 1963), that enable detection of invisible conformational states populated to as low as ~ 0.1% by manipulation of the visible state magnetization. These methods have been adapted and developed to study various biomolecular processes including folding, conformational exchange, ligand binding and aggregation (Anthis and Clore 2015; Gopalan et al. 2018a, b; Palmer and Koss 2019; Palmer et al. 2001; Rangadurai et al. 2019; Sekhar and Kay 2013; Tugarinov and Clore 2019; Vallurupalli et al. 2017; Yuwen et al. 2018a, b; Zhuravleva and Korzhnev 2017). The choice of the specific NMR technique appropriate for a given study is largely dictated by the timescale of the exchange process, with biomolecular interconversions ranging between tens of μs to seconds now amenable to investigation (Gopalan et al. 2018a, b; Massi et al. 2005; Rangadurai et al. 2019; Reddy et al. 2018; Vallurupalli et al. 2012; Yuwen et al. 2018a, b). In favourable cases structural models (Sanchez-Medina et al. 2014; Sugase et al. 2007) and even atomic resolution structures of the minor states can also be obtained (Bouvignies et al. 2011; Grey et al. 2003; Korzhnev et al. 2010; Neudecker et al. 2012). Insights into the shape of the free energy surface and how proteins explore the surface in performing a variety of functions can also be deduced from the experimentally detected states and interconversion rate constants (Bezsonova et al. 2006; Korzhnev et al. 2007; Sekhar et al. 2014; Tiwari et al. 2021), particularly in conjunction with computational techniques (Chung et al. 2015; Kukic et al. 2017; Vallurupalli et al. 2016).

In most NMR studies exchange data have been interpreted using a two-state interconversion model. Analysis using exchange models involving three or more conformational states remains a challenge since the experimental data is often not of sufficient quality to robustly extract the exchange parameters, or if it is, the χ^2 fitting surface can be rugged, further complicating the fitting of accurate interconversion rates and populations of states. Consequently, new NMR techniques and analysis strategies are actively being developed to study biomolecular conformational exchange processes involving multiple states (Grey et al. 2003; Korzhnev et al. 2005; Koss et al. 2017; Lim et al. 2014; Overbeck et al. 2023; Palmer and Koss 2019; Tiwari et al. 2021; Vallurupalli et al. 2019).

The CEST class of experiments (van Zijl and Yadav 2011; Ward et al. 2000) that were originally developed over six decades ago to study slow exchange between 'visible' states in small molecules (Forsen and Hoffman 1963) have now emerged as a powerful tool to study biomolecular conformational exchange between 'visible' and 'invisible' conformers (Vallurupalli et al. 2017). In CEST-based experiments an intensity profile is obtained for each site probed in the biomolecule, comprising a major dip at the resonance position of the spin in the major state, and smaller dips centred at resonance frequencies of the corresponding spin in the minor state conformations. Recent studies have established that CEST experiments can also be used to study exchange processes occurring on the intermediate to fast timescale in which case the CEST intensity profile does not contain well-separated dips but, often, a single asymmetric dip that can be analysed to study biomolecular dynamics occurring on the 100 μs timescale (Khandave et al. 2023; Rangadurai et al. 2020). Additionally, we have shown that the width of the minor state dip can be used to uncover other sparsely populated states that are in intermediate to fast time-scale exchange with the minor state, even when they do not give rise to distinct dips in CEST profiles (Tiwari et al. 2021). It is this particular case that we wish to further examine here, focusing on whether additional information can be used to achieve robust fits using three-state exchange models without a priori knowledge of the exchange process.

The 71 residue four helix bundle FF domain from human HYPA/FBP11 (WT FF) and a large number of FF mutants have emerged as model systems for protein folding studies, and have been extensively investigated using stopped flow (Jemth et al. 2004, 2008) and NMR techniques (Korzhnev et al. 2007, 2010). Burst phase analysis detected folding intermediates for 32 out of the 33 FF mutants (Jemth et al. 2008). Although a folding intermediate was not detected for the A39G FF domain by fluorescence, our CEST studies confirmed that at 1 °C this variant folds from the unfolded (U) state to the folded conformer (F) via two intermediates I1 (p_{I1} ~ 0.3%, lifetime ~ 0.2 ms) and I2 (p_{I2} ~ 0.2%, lifetime ~ 0.7 ms) along two separate pathways (Tiwari et al. 2021). Here we re-examine the folding pathway of WT FF, where a previous CPMG study defined a single on-pathway folding intermediate, I1, (Korzhnev et al. 2007, 2010) using ^{15}N-CEST. We show that data recorded at 15 °C, where the exchange between states varies from ~ 1100 s^{-1} (F,I2) to ~ 5000 s^{-1} (I1,I2), clearly report on both I1 and I2 intermediates despite the fact that CEST profiles with only a single minor dip are observed. While multiple three-state exchange models satisfy the data, a unique solution involving exchange between states F, I1 and I2 is obtained from analysis of the ^{15}N CEST data by introducing the temperature dependence of the positions of the minor state dips obtained from a simple two-state analysis of ^{15}N CEST profiles recorded at different temperatures. This solution is obtained without performing an extensive grid search over parameter space, suggesting that CEST data may prove more robust than the corresponding CPMG profiles in the analysis of some multi-state (> 2) systems, even when exchange rates are in the many hundreds to thousands per second.

Materials and methods

Protein samples

NMR samples consisted of approximately 2 mM [U-^{15}N] protein (WT FF or A39G FF) dissolved in 50 mM sodium acetate, 100 mM NaCl, 2 mM EDTA, 2 mM NaN_3, (5% A39G FF; 10% WT FF) D_2O (pH 5.7). [U-^{15}N] A39G FF and WT FF were over-expressed in *Escherichia coli* BL21(DE3) cells transformed with the appropriate plasmid grown in M9 media with $^{15}NH_4Cl$ as the sole nitrogen source and purified as described previously (Tiwari et al. 2021; Vallurupalli et al. 2009).

NMR spectroscopy

All NMR experiments were carried out on a 700 MHz (16.4 T) Bruker Avance III HD spectrometer equipped with a cryogenically cooled triple resonance probe. The ^{15}N CEST experiments were recorded using a pulse sequence (Vallurupalli et al. 2012) in which ^{1}H decoupling is carried out during the T_{EX} period using 90x240y90x composite inversion pulses (Levitt 1982), thus effectively reducing the ^{15}N–^{1}H spin-system to an isolated ^{15}N spin. Each two-dimensional ^{15}N–^{1}H plane was recorded with 24 complex points (16.9 ppm sweep-width) in the indirect ^{15}N dimension. Additional details are listed in Table S1. The strength of the ^{15}N B_1 field applied during the T_{EX} period was calibrated using the nutation method (Guenneugues et al. 1999).

Data analysis

^{15}N CEST data were processed using the *NMRPipe* software package (Delaglio et al. 1995), with *Sparky* used to visualize and label peaks (Goddard and Kneller 2008; Lee et al. 2015) in the ^{15}N–^{1}H correlation maps, and *PINT* used to extract peak intensities from the ^{15}N–^{1}H datasets (Ahlner et al. 2013). *ChemEx* (Bouvignies 2011), that numerically integrates (Korzhnev et al. 2004) the Bloch–McConnell equations (McConnell 1958) for various exchange models, was used to obtain the best-fit exchange parameters by minimizing the target function, $\chi^2 = \sum_{i=1}^{N} \left(\frac{I_{Exp,i} - I_{Calc,i}}{\sigma_i} \right)^2$. Here I_{Exp} is the measured experimental intensity of a peak, I_{Calc} is the corresponding calculated intensity, σ is the uncertainty in the experimental measurement and the summation extends over all the experimental measures (i) being considered in the fitting process. For each site at a given temperature σ was estimated from the scatter in the intensities in the flat parts of the ^{15}N CEST profiles recorded at the lowest B_1 value because CEST profiles recorded with high B_1 values sometimes did not contain flat regions (Khandave et al. 2023; Vallurupalli et al. 2012). The minimum value of σ was set to 0.2%. Uncertainties in the best-fit parameters were determined using 100 bootstrap or Monte-Carlo trials (Choy et al. 2005; Press et al. 1992). In the bootstrap procedure "new" realisations of the experimental datasets were generated by selecting experimental data points randomly with repetition from each ^{15}N CEST profile, such that the total number of datapoints remains constant. The intensity from the reference plane was always included in the datasets. In the Monte Carlo procedure synthetic datasets were generated by adding random Gaussian error corresponding to the uncertainty in the measured intensities to the intensities calculated using the best-fit parameters.

In the two-state analysis of the ^{15}N CEST data the global fitting parameters that are common for all residues are the exchange rate and the minor state population. The residue specific fitting parameters were the major and minor state chemical shifts, R_1 and R_2 values of spins in the major state, and in some cases, as described in the text, the R_2 values of spins in the minor state (in other cases fits were carried out with the same R_2 values for corresponding spins in both states). The value of R_1 for a given spin was constrained to be the same for both states.

When analysing the ^{15}N CEST data using three-state exchange models the global fitting parameters were the two minor state populations and the three exchange rates, while the residue specific fitting parameters were the major and minor state chemical shifts, and major state R_1 and R_2 values. R_1 and R_2 values were constrained to be the same for all three states. To prevent unphysical solutions $|\Delta\varpi_{FM1} = \varpi_{M1} - \varpi_F|$ and $|\Delta\varpi_{M1M2}|$ were constrained to be ≤ 20 ppm, where M1 and M2 refer to different minor states, as described in the "Results and discussion" section. $\Delta\varpi_{FM1}$ was initialised to $\Delta\varpi_{FM}$ obtained from two-state (F $\leftrightharpoons$ M) fits of the ^{15}N CEST data. When the best fit procedure was carried out in the absence of $\Delta\varpi_{M1M2}$ sign information $\Delta\varpi_{M1M2}$ was initialised to 0 ppm, i.e., both ϖ_{M1} and ϖ_{M2} at the minor state dip position in the ^{15}N CEST profiles. When the sign of $\Delta\varpi_{M1M2}$ was available, $\Delta\varpi_{M1M2}$ was initialised to $+2$ (-2) ppm when $\Delta\varpi_{M1M2}$ was positive (negative).

Synthetic ^{15}N CPMG data were generated for an isolated spin ½ nucleus by propagating the Bloch–McConnell equations according to the $^1H^N$ decoupled ^{15}N CPMG sequence (Hansen et al. 2008). The Liouvillian was constructed using the CEST derived three-state kinetic parameters and $\Delta\varpi_{FM1}$ and $\Delta\varpi_{M1M2}$ values. To minimise the off-resonance effects, ϖ_F was set on resonance with the carrier and the length of the refocusing π pulses was 2 µs. R_1 and R_2 were set to 1 and 10 s^{-1} for all residues in all states, T_{EX} was set to 20 ms, and ν_{CPMG} values ranged from 50 to 1000 Hz. To account for noise in the measurements Gaussian random errors corresponding to the 2% of the effective relaxation rates ($R_{2,eff}$) were added to the calculated intensities. When 2% of the

effective relaxation rate was less than 0.4 s^{-1} the minimum error in $R_{2,eff}$ was set to 0.4 s^{-1}.

When analysing the synthetic ^{15}N CPMG relaxation-dispersion profiles using a two-state exchange model, the global fitting parameters were the minor state population and the exchange rate; residue specific fitting parameters were the minor state chemical shift and the major state R_2 value. The ground state chemical shift was fixed to the input value, R_2 was constrained to be the same for both states, R_1 was the same for both states and fixed to the input value. Here input values refer to the values used to generate the synthetic data.

In the case of WT FF, ^{15}N CEST data from 11 sites {K26, K41, I43, S50, L52, A53, L55, S56, K59, V67, Q68} showed clear evidence of exchange (see "Results and discussion" section) at 15 °C. Unless specified, these 11 residues, termed "set11", were used for the analysis at all temperatures. In the case of A39G FF data from 13 sites {T13, K26, K28, R29, N33, E37, K41, M42, I43, S50, L52, L55, L59} were analysed, chosen because $\left|\Delta\varpi_{FI1}\right| \geq 4$ ppm (Tiwari et al. 2021).

Results and discussion

The width of the minor state CEST dip is sensitive to interconversion with additional minor conformers

In a typical CEST experiment chemical exchange is quantified by recording the evolution of longitudinal (Z) magnetization for a period of fixed duration, T_{EX}, during which a weak B_1 field is applied over a range of frequencies (typically one frequency at a time per experiment), 'searching' for resonance frequencies of spins in invisible state(s). For simplicity we start by considering a two-state exchange reaction ($A \underset{k_{AB}}{\overset{k_{BA}}{\rightleftharpoons}} B$) in which the major state A exchanges slowly with the minor state B ($k_{ex,AB}/\left|\Delta\omega_{AB}\right| \ll 1$) (Cavanagh et al. 2006). In what follows we define $k_{ex,AB} = k_{AB} + k_{BA}$, with the fractional population of state B(A) given by $p_B = k_{AB}/k_{ex,AB}$ ($p_A = k_{BA}/k_{ex,AB}$) so that $p_A + p_B = 1$. The chemical shifts (ppm) of states A and B are defined as ϖ_A and ϖ_B, respectively, with $\Delta\varpi_{AB} = \varpi_B - \varpi_A$. Similarly, ω_A and ω_B denote the resonance frequencies (rad/s) of states A and B, respectively ($\Delta\omega_{AB} = \omega_B - \omega_A$). As mentioned above, the B_1 field is applied at specific offsets to cover the entire chemical shift range of interest and a plot of the normalised intensity (I/I_0) vs the frequency at which the B_1 field is applied (ϖ_N for ^{15}N CEST) produces a profile with dips at both ϖ_A and ϖ_B, arising from states A and B respectively, that are in exchange with each other. This is illustrated in Fig. 1a where the $B_1 = 52$ Hz ^{15}N CEST profile that has been calculated for an exchange process with $k_{ex,AB} = 75$ s^{-1}, $p_B = 2\%$, $\varpi_A = 0$ ppm and $\varpi_B = 7$ ppm (16.4 T) has clear intensity dips at 0 and 7 ppm. Here I_0 is the intensity obtained from an experiment without the T_{EX} delay. The exchange parameters ($k_{ex,AB}$ and p_B), the chemical shifts (ϖ_A, ϖ_B), and the transverse relaxation rates ($R_{2,A}$, $R_{2,B}$) of each spin in the two interconverting states can be obtained by analysing CEST intensity profiles recorded using different B_1 values that typically range between ~ 5 and 300 Hz (Rangadurai et al. 2020; Yuwen et al. 2018a, b). CEST experiments have been developed to study exchange at all backbone and most side-chain sites (Bouvignies and Kay 2012; Bouvignies et al. 2014; Cabrera Allpas et al. 2023; Hansen and Kay 2014; Karunanithy et al. 2020; Pritchard and Hansen 2019; Tiwari and Vallurupalli 2020; Vallurupalli et al. 2012; Vallurupalli and Kay 2013; Yuwen et al. 2017), so that NMR spectra of the minor states (typically the predominant minor conformer) of a protein can be reconstructed and in some cases detailed structural information obtained (Madhurima et al. 2023). In cases where exchange is more complex than two-state, additional minor dips can be obtained so long as each exchange process is slow on the chemical shift timescale, as illustrated in Fig. 1b where separate dips are observed for spins in states B and C.

The T_{EX} delay in the CEST experiment is usually in the 300 to 1000 ms window while the corresponding delay in a CPMG experiment is in the 20 to 100 ms range. The CEST experiment is thus sensitive to exchange processes that are either too slow to be detected by CPMG or involving minor states with populations about an order of magnitude smaller (~ 0.1%) than those typically detected by analysis of CPMG profiles (~ 1%) (Ramanujam et al. 2019; Rangadurai et al. 2019; Tiwari et al. 2021). What is less commonly appreciated is that CEST can be used effectively to study multi-state interconversion processes where exchange between the invisible states is rapid, as for the WT FF domain considered here, so that only a single minor state dip is observed. To illustrate this, we have calculated a CEST profile for a three-state interconverting system in which the third state C ($\varpi_C = 4$ ppm) is in fast exchange with state B. While there is no dip at ϖ_C, the B state dip at ϖ_B in the case of slow two-state exchange (Fig. 1a) has now broadened and shifted towards ϖ_C (compare Fig. 1c with Fig. 1a). This provides a simple means for identifying exchange between minor states, termed minor exchange (Trott and Palmer 2004), because the CEST profile of Fig. 1c cannot be analysed using the simple condition of equal transverse relaxation rates, $R_{2,A} = R_{2,B}$ (Tiwari et al. 2021; Vallurupalli et al. 2012; Vallurupalli and Kay 2013). The condition $R_{2,A} = R_{2,B}$ is valid, in general, only for a two-site exchange process where spins relax with similar transverse relaxation rates, such as for the interconversion between a folded state and a folding intermediate, but not when the 'CEST-visible' minor state exchanges with 'CEST-invisible' conformers which would increase the effective relaxation rate of the CEST-visible minor state,

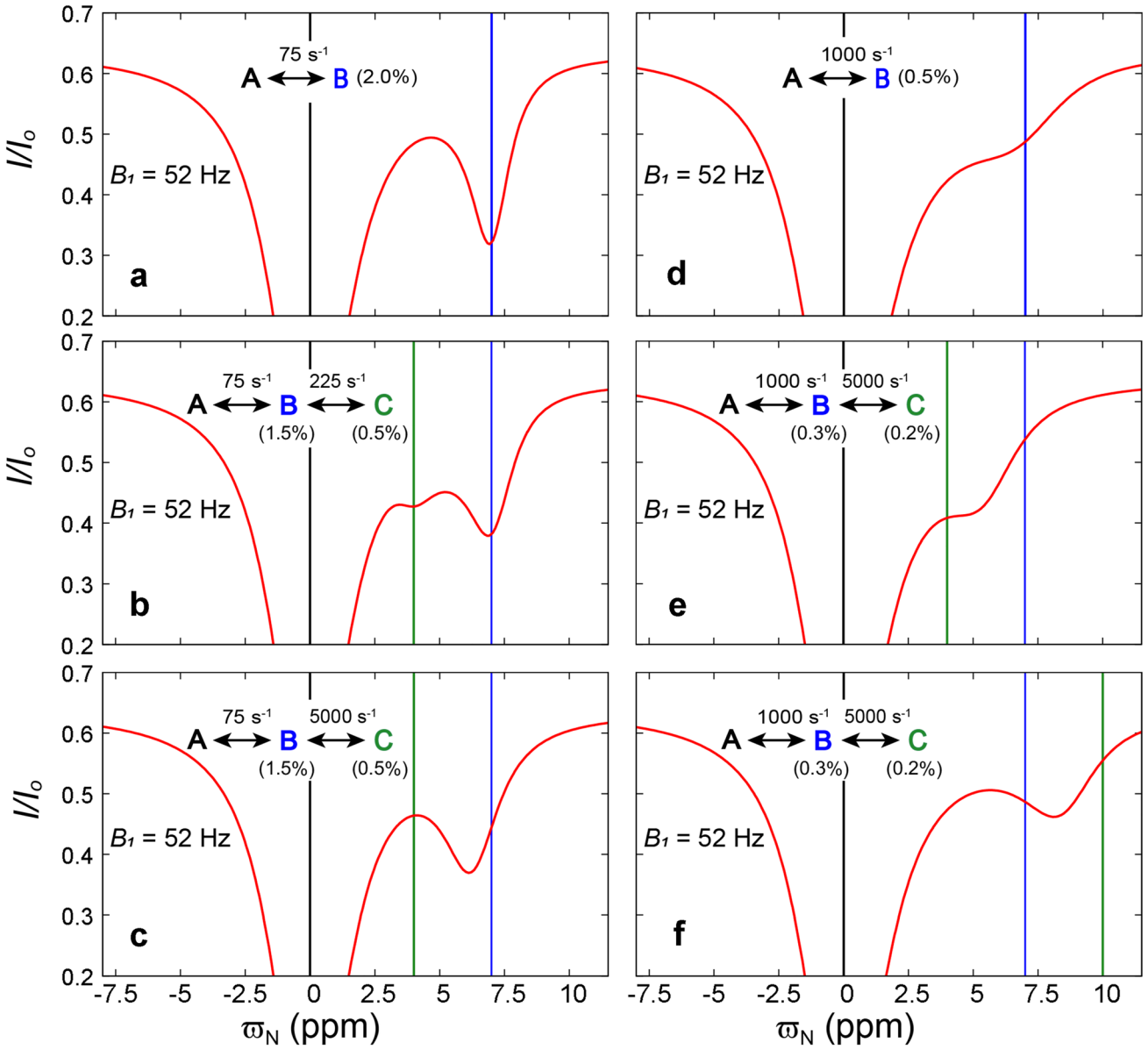

Fig. 1 ^{15}N CEST profiles calculated in the case of two-state (**a**, **d**) and three-state exchange (**b**, **c**, **e**, **f**), with exchange models and associated parameters as indicated. The profiles were calculated using the following parameters: $B_0 = 16.4$ T, $B_1 = 52$ Hz, $T_{EX} = 450$ ms, $R_{1,A} = R_{1,B} = R_{1,C} = 1$ s^{-1}, $R_{2,A} = R_{2,B} = R_{2,C} = 10$ s.$^{-1}$, $\varpi_A = 0$ ppm, $\varpi_B = 7$ ppm and $\varpi_C = 4$ ppm (or $\varpi_C = 10$ ppm in panel **f**). Note that when minor states B and C exchange in the intermediate to fast regime only a single minor dip is observed (**c**, **e**, **f**) and its position is sensitive to the B, C interconversion (compare **a** with **c**, and **d** with **e** and **f**; that is the minor dip contains information about both states B and C)

and certainly not in the case of aggregation where one state is a monomer and the second a large aggregate (Tugarinov and Clore 2019). Exchange between species with very different masses but identical chemical shifts (Allerhand and Thiele 1966) are studied using the DEST class of experiments (Tugarinov and Clore 2019).

Figure 1a–c show examples where the interconverting states A and B are in slow exchange on the NMR chemical shift timescale, believed to be an optimal case for CEST. We wondered whether the linewidths of the minor dips could still be used as an indicator of additional exchange processes between CEST-visible and CEST-invisible conformers when the A, B interconversion rate increases and where the populations of the minor species are reduced. To this end we calculated ^{15}N CEST profiles for systems exchanging on the millisecond timescale (Fig. 1d–f). In the case of a two-site exchanging system with $k_{ex,AB} = 1000$ s^{-1} and $p_B = 0.5\%$ the ^{15}N CEST intensity profile (Fig. 1d) has a large

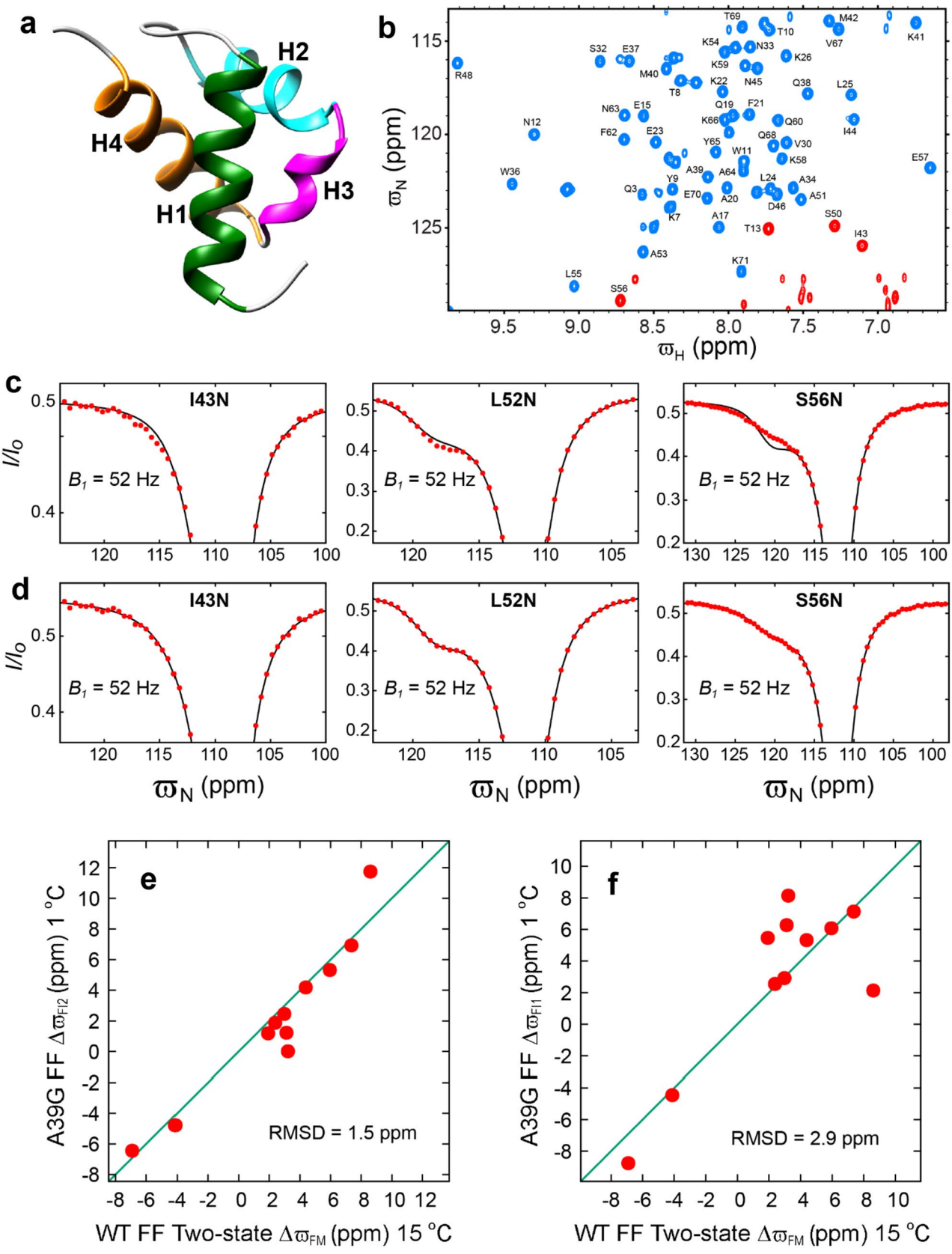
a
H2
H4
H3
H1
b
ϖN (ppm)
ϖH (ppm)
c
I43N
L52N
S56N
I/Io
B1 = 52 Hz
d
ϖN (ppm)
e
A39G FF Δϖ FI2 (ppm) 1 °C
WT FF Two-state Δϖ FM (ppm) 15 °C
RMSD = 1.5 ppm
f
A39G FF Δϖ FI1 (ppm) 1 °C
RMSD = 2.9 ppm

◂**Fig. 2** ^{15}N CEST establishes that WT FF populates more than one minor state at 15 °C. **a** The native structure of the FF domain (PDB: 1UZC; Allen et al. 2002) has four helices: H1 (T13 to K28: green), H2 (S35 to N45, cyan), H3 (D46 to L52, magenta), and H4 (K54 to T69, orange). **b** The ^{15}N–^{1}H correlation map of WT FF (15 °C, 16.4 T) is well resolved; peaks are labelled according to the residue from which they arise. Red peaks are aliased in the ^{15}N dimension. **c** A simple two-state exchange model where corresponding spins in the major and minor states have the same R_2 value does not account for the (B_1 = 20.8 and 52 Hz) ^{15}N CEST data (χ^2_{red} = 1.9). **d** Fits are greatly improved when allowing for different major and minor state R_2 values (χ^2_{red} = 0.74, $k_{ex,FM}$ = 1020 ± 15 s.$^{-1}$ and p_M = 0.5 ± 0.01%). In **c** and **d**, the red circles correspond to experimental measures while the black line is calculated using the best fit parameters. Comparison of WT FF two-state $\Delta\varpi_{FM}$ values with A39G FF $\Delta\varpi_{FI2}$ (**e**) and A39G FF $\Delta\varpi_{FI1}$ (**f**) values, as determined previously (Tiwari et al. 2021)

dip at 0 ppm (ϖ_A) and a shoulder at 7 ppm (ϖ_B), in contrast to the case when $k_{ex,AB}$ = 75 s^{-1} (Fig. 1a) where distinct dips are present at 0 and 7 ppm. Nonetheless, on introducing state C with $k_{ex,BC}$ = 5000 s^{-1} and ϖ_C = 4 ppm ($\Delta\varpi_{BC}$ = − 3 ppm), the minor state dip becomes slightly more narrow and shifts towards ϖ_C (Fig. 1e), while if $\Delta\varpi_{BC}$ = 3 ppm, a sharpened (relative to the case where $\Delta\varpi_{BC}$ = − 3 ppm) dip is observed at ~ 8 ppm, again shifted in the direction of the resonance position of the spin in state C (Fig. 1f). It is clear that for three-state interconverting systems where only a single minor dip is observed valuable information about the exchange between the minor states, in particular chemical shifts, is encoded in the minor dip linewidth (and position). We show below that this information, at least in some cases, can be sufficient to extract out all of the parameters defining the exchange process.

WT FF populates more than two states at 15 °C

Figure 1 shows that even in cases where only a single minor dip is observed in CEST profiles that report on multiple-site (> 2) interconversions insight into the exchange process can still be obtained from the width of the minor dip. We wondered whether an analysis of CEST profiles recorded on the WT FF domain where only single minor dips were observed might, therefore, reveal the pair of intermediates I1 and I2 that were detected in previous studies of the A39G FF domain (Tiwari et al. 2021). As mentioned in the Introduction, CPMG dispersion profiles of WT FF could be well-fit to a two-site exchange process (F ↔ I1), with no evidence of a second intermediate. Figure 2a shows the structure of the native state of the WT FF domain that consists of a disordered N-terminal tail (residues 1–10) followed by four helices (Allen et al. 2002). The amide ^{15}N–^{1}H correlation map of WT FF is very well resolved at 15 °C (Fig. 2b, 16.4 T) and ^{15}N CEST profiles could be quantified for 55 out of 59 non-proline ordered residues (11–71). Eleven residues showed clear evidence of exchange (referred to as set11 and listed in "Materials and methods" section) since a model that did not include such contributions could not account for ^{15}N CEST profiles recorded with B_1 = 20.8 and 52 Hz ($\chi^2_{red} \geq 5$). A global (common exchange rates and populations for all sites) two-state exchange model in which the F state exchanges with a single invisible minor state (M), subject to the constraint that the transverse relaxation rates for corresponding spins in the interconverting conformers are the same ($R_{2,M}$ = $R_{2,F}$), also could not explain the ^{15}N CEST data (χ^2_{red} = 1.9, B_1 = 20.8 and 52 Hz; Fig. 2c) for the set11 residues. However, when the constraint on the R_2 values is not imposed, the two-state model accounts for the ^{15}N CEST data (χ^2_{red} = 0.74; Fig. 2d) with $k_{ex,FM}$ = 1020 ± 15 s^{-1} and p_M = 0.50 ± 0.01%. The large differences in $R_{2,M}$ and $R_{2,F}$ rates observed for some residues in the fits is not consistent with two-state exchange in this case as folded and folding intermediate conformations are expected to have similar tumbling times, but rather reflects a more complex exchange process. Notably, the best-fit two-state $\Delta\varpi_{FM}$ values are in reasonable agreement (RMSD 1.5 ppm; Fig. 2e) with the A39G FF $\Delta\varpi_{FI2}$ values obtained previously (Tiwari et al. 2021) but are not in agreement (RMSD 2.9 ppm; Fig. 2f) with the A39G FF $\Delta\varpi_{FI1}$ values, suggesting that WT FF populates the I2 state at 15 °C.

Multiple three-state solutions satisfy the WT FF ^{15}N CEST data recorded at 15 °C

Having established that WT FF exchanges between the folded state and at least two minor states we proceeded to analyse the 15 °C ^{15}N CEST data (B_1 = 20.8, 52, 104 and 208 Hz) from the 11 set11 residues using a triangular three-state model in which the major state (F) and the two minor states (M1 and M2) interconvert with each other. The triangular three-state model, subject to the constraint $R_{2,M1}$ = $R_{2,M2}$ = $R_{2,F}$, fits the data well (χ^2_{red} = 0.97) and p_{M1} + p_{M2} (0.5 ± 0.01%) is in good agreement with the minor state population obtained above (p_M = 0.5%). In Fig. 3, the results from 100 bootstrap trials are plotted and it is clear from Fig. 3a that the obtained p_{M1} (0.3 ± 0.03%) and p_{M2} (0.2 ± 0.03%) values are correlated, with the relative populations of M1 and M2 (p_{M1}/p_{M2}) varying from 1 to 2.75 (Fig. 3b; note that the two minor states are labelled M1 and M2 such that $p_{M1} > p_{M2}$). The lack of a unique three-state solution is further exemplified in Fig. 3c, where the best fit values of $\Delta\varpi_{FM1}$ and $\Delta\varpi_{M1M2}$ obtained for each residue from the 100 bootstrap trials are plotted. Unlike p_{M1} and p_{M2} that are correlated and adopt a range of solutions (Fig. 3a), $\Delta\varpi_{FM1}$ and $\Delta\varpi_{M1M2}$ are sometimes also correlated but tend to cluster around two distinct ($\Delta\varpi_{FM1}$, $\Delta\varpi_{M1M2}$) pairs for several sites; the reason for plotting $\Delta\varpi_{M1M2}$ values rather than the customary $\Delta\varpi_{FM2}$ shift differences will become clear in the next section. The lack of a unique three-state

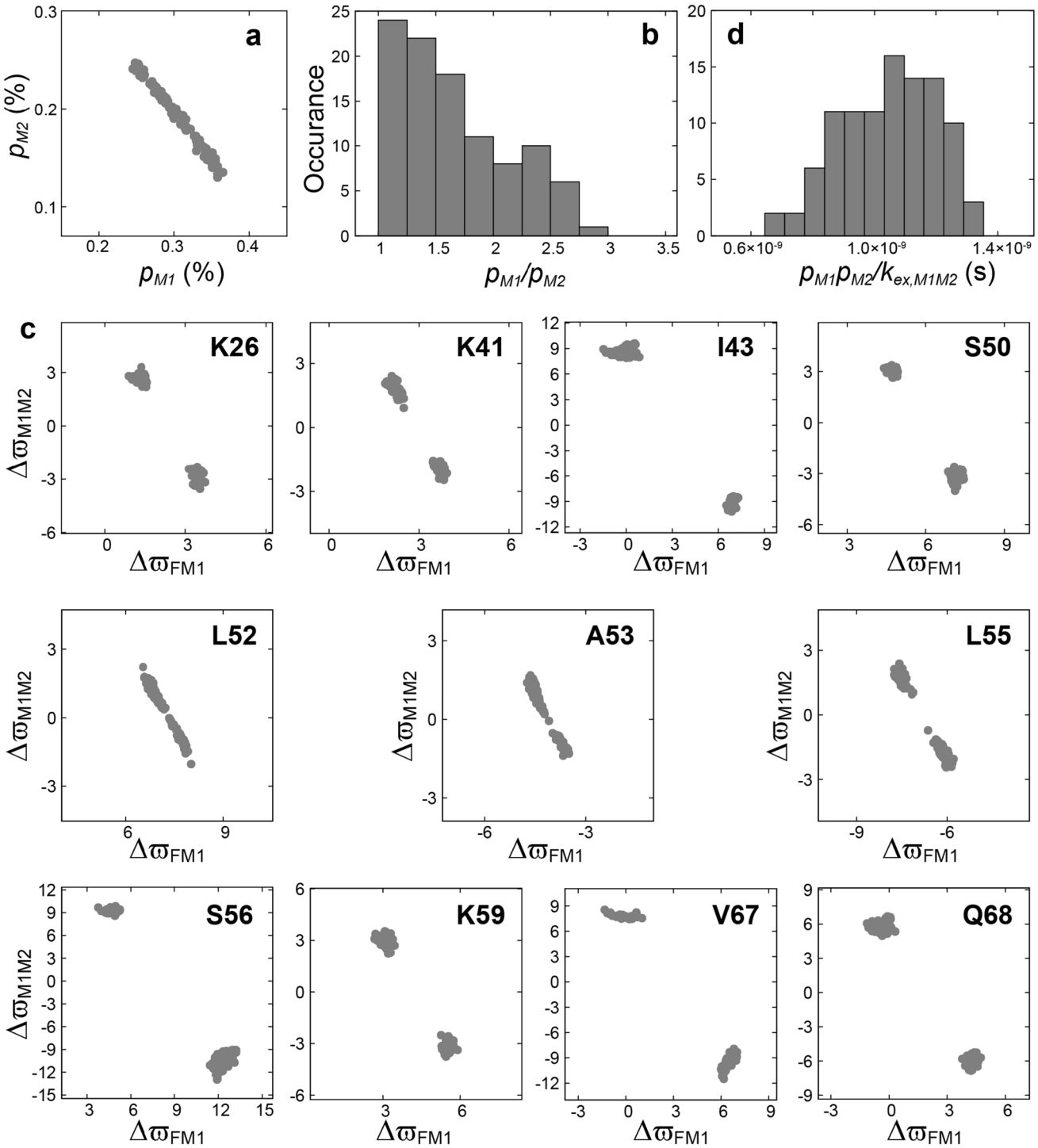

Fig. 3 Unique exchange parameters cannot be extracted when the WT FF ^{15}N CEST data recorded at 15 °C is analysed using a triangular three-state exchange model. **a** Plot of p_{M1} and p_{M2} generated from 100 bootstrap trials. **b** Histogram showing the distribution of p_{M1}/p_{M2} obtained from 100 bootstrap trials. **c** $\Delta\varpi_{FM1}$ and $\Delta\varpi_{M1M2}$ values (ppm) obtained from 100 bootstrap trials for different sites, as indicated. **d** Distribution of $p_{M1}p_{M2}/k_{ex,M1M2}$ obtained from 100 bootstrap trials

solution reflects the presence of multiple minima along the χ^2_{red} surface and the rugged energy landscape that prevent convergence to a global minimum. In previous analyses of CPMG data recorded on systems undergoing three-site chemical exchange the global χ^2_{red} minimum could only be obtained through extensive grid search procedures

(Korzhnev et al. 2004; Neudecker et al. 2006). In some cases, noise in the data can lead to similar or better-quality fits in spurious minima complicating extraction of the correct exchange parameters (Korzhnev et al. 2004; Neudecker et al. 2006). These complications were circumvented to a large extent in a previous study of the folding of A39G FF using ^{15}N CEST experiments where analysis of the data utilised the I1 chemical shifts based on CPMG studies (Korzhnev et al. 2010) as well as the predicted U state chemical shifts (Nielsen and Mulder 2018) as initial guesses with only a limited grid search to determine the I2 state chemical shifts (Tiwari et al. 2021). The goal of the study here is to ascertain whether it is possible to reconstruct the energy landscape of the WT FF domain without *a prior* knowledge of the chemical shifts of any of the intermediate states and without resorting to a computationally expensive grid search.

Degeneracy in the sign of $\Delta\varpi_{M1M2}$ leads to multiple three-state solutions

As a first step to develop a protocol for obtaining accurate three-state exchange parameters we attempted to understand why multiple sets of parameters could satisfy the ^{15}N CEST data (Fig. 3). As mentioned before $\Delta\varpi_{FM1}$ and $\Delta\varpi_{M1M2}$ can be correlated but are typically clustered around two sets of values. Notably the clusters are centred about $\Delta\varpi_{M1M2}$ values with similar magnitudes but opposite signs (Fig. 3c); that is $|\Delta\varpi_{M1M2}|$ is reasonably well defined but the sign of $\Delta\varpi_{M1M2}$ is not. The degeneracy can be understood by recognizing that the width of the visible minor state dip (state M1) is used to detect the CEST-invisible state M2. For an M1 $\leftrightharpoons$ M2 interconversion process that is reasonably fast on the NMR chemical shift timescale, as is the case for WT FF (see below), the observed minor state dips (from M1) will be broadened by an amount proportional to $p_{M1}p_{M2}\Delta\omega^2_{M1M2}/k_{ex,M1M2}$ (Palmer 2004). The width, thus, depends on $\Delta\varpi^2_{M1M2}$ and not on $\Delta\varpi_{M1M2}$, and the necessary sign information to correctly position resonance frequencies of states M1 and M2 is not available (Gopalan and Vallurupalli 2018; Skrynnikov et al. 2002; Vallurupalli et al. 2011). As $p_{M1}p_{M2}/k_{ex,M1M2}$ is reasonably well defined by the fitting procedure ($1.04 \pm 0.15 \times 10^{-9}$ s; Fig. 3d), $\Delta\varpi_{M1M2}$ clusters around two values with opposite sign rather than adopting a continuous distribution of values. Neglecting the effect of the F state, when the exchange between states M1 and M2 is fast, the minor state dip position in the ^{15}N CEST profiles is shifted from ϖ_{M1} towards ϖ_{M2} (compare Fig. 1a and c) by $\approx (p_{M2}\Delta\varpi_{M1M2})/(p_{M1}+p_{M2})$, so that the position of the minor state dip occurs at $\varpi_{M1}+(p_{M2}\Delta\varpi_{M1M2})/(p_{M1}+p_{M2})$ and not ϖ_{M1} as would be the case in the absence of the M1 $\leftrightharpoons$ M2 interconversion. In order to fit the position of the minor state dip when the data only constrains $|\Delta\varpi_{M1M2}|$ and not $\Delta\varpi_{M1M2}$, a pair of ϖ_{M1} values results, $\{\varpi_{M1A}, \varpi_{M1B}\}$, such that $\varpi_{M1A}+(p_{M2}\Delta\varpi_{M1M2})/(p_{M1}+p_{M2}) = \varpi_{M1B} - (p_{M2}\Delta\varpi_{M1M2})/(p_{M1}+p_{M2})$. Hence $\Delta\varpi_{FM1}$ and $\Delta\varpi_{M1M2}$ are clustered around two distinct pairs of values. This is illustrated in Fig. 4, where a three-state (A $\leftrightharpoons$ B $\leftrightharpoons$ C) model was fit as a function of $\Delta\varpi_{BC}$ to CEST data generated with $\varpi_A = 0$ ppm, $\varpi_B = 6$ ppm, $\varpi_C = 3$ ppm and exchange parameters as illustrated in Fig. 4a. The χ^2_{red} vs $\Delta\varpi_{BC}$ plot has two minima (Fig. 4a), with the first occurring at the correct $\Delta\varpi_{BC}$ value of -3 ppm, in which case the best fit $\Delta\varpi_{AB} = 6$ ppm (Fig. 4b), while the second minimum occurs at $\Delta\varpi_{BC} = 2.6$ ppm (~3 ppm) to produce a best fit $\Delta\varpi_{AB}$ of 3.4 ppm (Fig. 4c). Note that for the second (false) minimum that occurs with the sign of $\Delta\varpi_{BC}$ inverted (~3 ppm vs. -3 ppm), $\Delta\varpi_{AB}$ is modified such that the best fit profile is nearly identical to the corresponding profile obtained with the correct fitted parameters (Fig. 4c). In Fig. 4a, the χ^2_{red} at the wrong minimum is higher by 0.36 than the value at the correct minimum and this difference reflects the fact that the exchange parameters were fixed to the input values during the fitting procedure. This small difference will be reduced or vanish while analysing experimental data as the exchange parameters are unknown and can only be simultaneously determined along with chemical shifts during the course of the fit. Global analysis of data from several residues will alleviate this problem to some extent but the two-fold degeneracy for each $\Delta\varpi_{M1M2}$ will remain so long as the M1, M2 interconversion is fast, as is the case when only a single minor state dip is observed for all residues.

The (relative) signs of $\Delta\varpi_{M1M2}$ can be obtained from the two-state analysis of ^{15}N CEST profiles recorded at multiple temperatures

While the width of the minor state dip does not depend on the sign of $\Delta\varpi_{M1M2}$, the position of the dip does (Fig. 1a–c). Hence the sign of $\Delta\varpi_{M1M2}$ can be determined if the ratio p_{M2}/p_{M1} is varied in a controlled manner in a set of experiments and the position of the minor state dip followed. As p_{M2}/p_{M1} increases the minor state dip moves towards ϖ_{M2} as illustrated in Fig. 5a, b, where the minor state dip that is close to ϖ_B (8 ppm) in Fig. 5a moves towards ϖ_C (3 ppm) in Fig. 5b when the ratio of the minor state populations p_C/p_B is increased from 0.25 (Fig. 5a) to 0.5 (Fig. 5b). The ratio of the minor state populations can be modulated by changing the pH, using additives or most conveniently by varying the temperature. This suggests that the sign of the difference between minor state chemical shifts can be obtained by analysing ^{15}N CEST profiles recorded at multiple temperatures using a two-state exchange model in which the transverse relaxation rates are not constrained. To empirically determine if this is the case, we initially analysed ^{15}N CEST profiles (B_1 ~20 and ~50 Hz; Table S1) recorded on

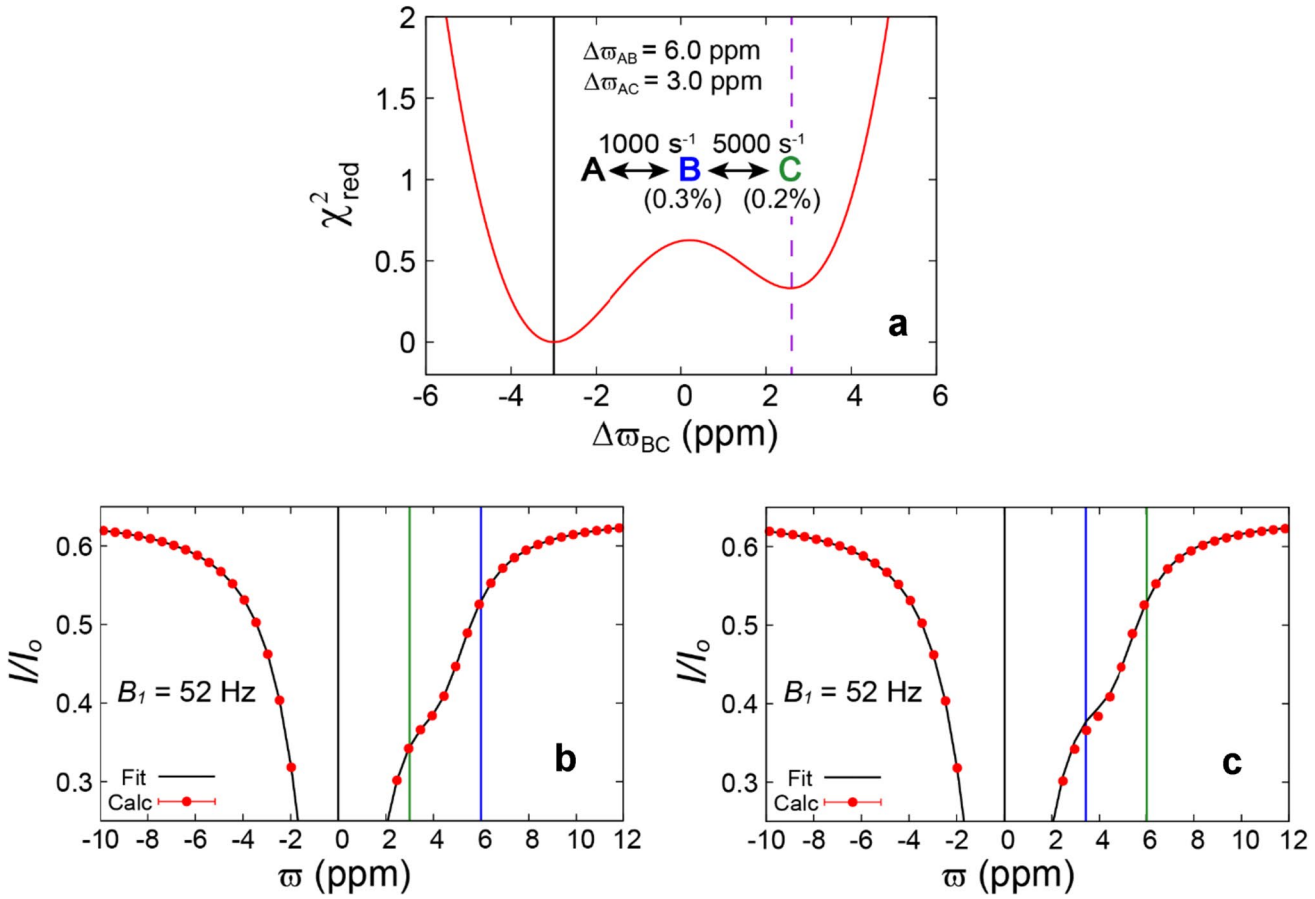

Fig. 4 The shape of the ^{15}N CEST profile is relatively insensitive to the sign of the chemical shift difference between the minor state resonances. **a** Synthetic ^{15}N CEST data were generated for the linear A ⇋ B ⇋ C exchange model as shown with ϖ_A= 0 ppm, ϖ_B= 6 ppm, and ϖ_C= 3 ppm, $R_{1,A} = R_{1,B} = R_{1,C} = 1$ s^{-1}, $R_{2,A} = R_{2,B} = R_{2,C} = 10$ s^{-1}, and fit to a three-state model as a function of $\Delta\varpi_{BC}$. The resulting χ^2_{red} vs $\Delta\varpi_{BC}$ plot contains two minima, with the deeper minimum occurring at the correct $\Delta\varpi_{BC}$ value of −3 ppm while a second more shallow minimum occurs at $\Delta\varpi_{BC}$ = 2.6 ppm (~3 ppm). Representative plots of the fits corresponding to the global and local minima are shown in **b** and **c** respectively. To make the χ^2_{red} vs $\Delta\varpi_{BC}$ plot ^{15}N CEST profiles (B_0 = 16.4 T) were generated with four B_1 (Hz)/T_{EX} (ms) values (20.8/475, 52/450, 104/350 and 208/350) and the resulting profiles subsequently fit. No noise was added but an uncertainty of 0.3% in the intensities was assumed to calculate the χ^2_{red} values. Three-state fits to the synthetic data were carried out with the exchange rates and populations fixed to the input values, while ϖ_A, ϖ_B, ϖ_C, $R_{1,A}$ and $R_{2,A}$ were allowed to vary. Constraints $R_{1,B} = R_{1,C} = R_{1,A}$ and $R_{2,B} = R_{2,C} = R_{2,A}$ were imposed during the fitting procedure

a sample of A39G FF at 1, 2.5, 5, 10 and 15 °C for which detailed folding studies have previously been published (Tiwari et al. 2021). In the case of A39G FF, the minor state dip in the ^{15}N CEST profiles arises largely due to the U state that in turn is in rapid exchange ($k_{ex,I1U}$ ~ 8500 s^{-1} at 1 °C) with the I1 state (Fig. 5c). Data at all five temperatures were analysed using a two-state model in which the F state exchanges with the U state. For all 13 sites analysed here $\Delta\varpi_{UI1}$ is negative and we find that for 12 sites the fitted two-state $\Delta\varpi_{FU}$ values monotonically decrease with temperature (become more negative) presumably because p_{I1}/p_U increases with temperature. On the other hand, if p_{I1}/p_U were to decrease with temperature, the behaviour seen in Fig. 5c would imply that all the $\Delta\varpi_{UI1}$ values are positive. For any new system studied the temperature dependence of p_{M2}/p_{M1} is not known, so that there are two possible values for each $\Delta\varpi_{M1M2}$. In the case of A39G FF and in the absence of any a priori knowledge there would be 2^{12} possible sets of signs for $\Delta\varpi_{UI1}$, as $\Delta\varpi_{UI1}$ for each residue can be either positive or negative. However, using the temperature dependence depicted in Fig. 5c (and neglecting prior knowledge about absolute signs) all of the 12 $\Delta\varpi_{UI1}$ values would be either positive or all would be negative. Of course, if the sign of $\Delta\varpi_{UI1}$ for one residue is known then the signs for all the other $\Delta\varpi_{UI1}$ values would be available as well. In principle, therefore, generating the correct signs for $\Delta\varpi_{M1M2}$ involves considering only two (and not 2^{12}) possibilities and choosing the best solution by comparing χ^2_{red} values obtained in fits of the CEST profiles. In practice, we will show below that there is no need to perform two fits and a grouping of

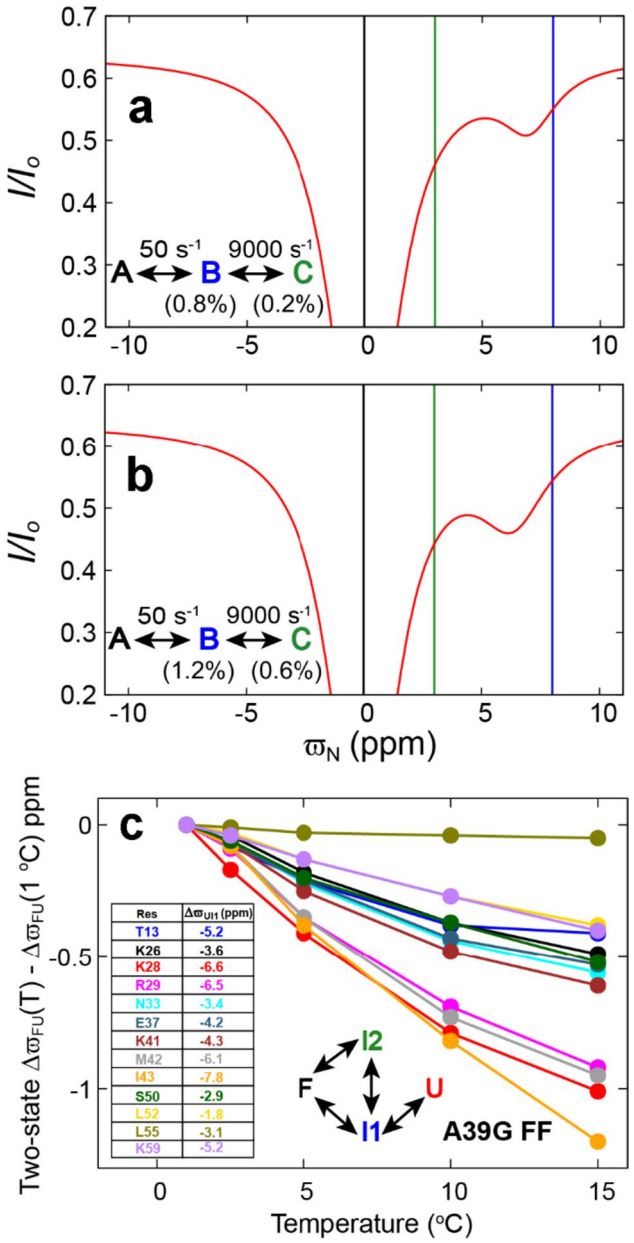

Fig. 5 The temperature dependencies of the minor state dip positions can be used to obtain the relative signs of the chemical shift differences between the minor state resonances. **a**, **b** ^{15}N CEST profiles calculated using the indicated exchange parameters, $B_0 = 16.4$ T, $B_1 = 52$ Hz, $T_{EX} = 450$ ms, $R_{1,A} = R_{1,B} = R_{1,C} = 1$ s^{-1}, $R_{2,A} = R_{2,B} = R_{2,C} = 10$ s^{-1}, $\varpi_A = 0$ ppm, $\varpi_B = 8$ ppm and $\varpi_C = 3$ ppm. The minor state dip that is close to ϖ_B in **a** shifts towards ϖ_C in **b** because p_C/p_B has increased from 0.25 in **a** to 0.5 (**b**). **c** Variation of the A39G FF two-state $\Delta\varpi_{FU}$ values as a function of temperature

residues according to $\frac{d\Delta\varpi_{M1M2}}{dTemp}$ is sufficient. Note that for L55 $\Delta\varpi_{FU}$ is temperature independent (Fig. 5c) so that the sign of $\Delta\varpi_{UI1}$ is not available from this data. This strategy of obtaining the relative signs of $\Delta\varpi_{M1M2}$ from the two-state analysis of ^{15}N CEST profiles recorded at multiple

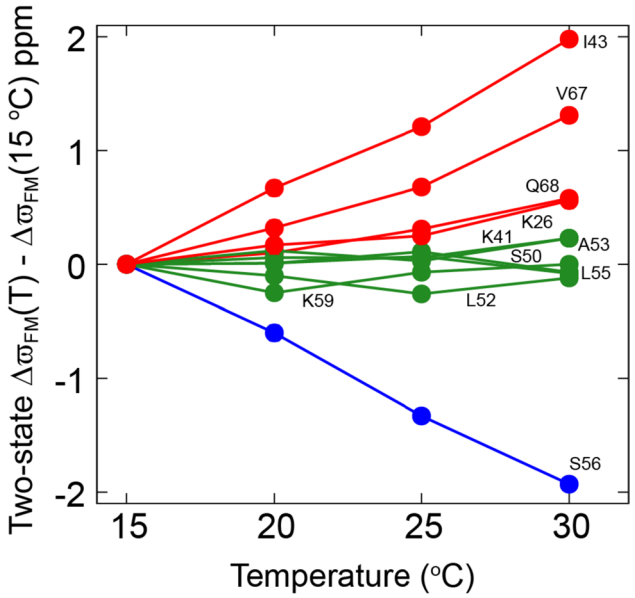

Fig. 6 Variation of the WT FF two-state $\Delta\varpi_{FM}$ values from different sites as a function of temperature. ^{15}N CEST data ($B_1 \sim 20$ and ~ 50 Hz; Table S1) recorded at 15, 20, 25 and 30 °C were analysed using a two-state model (F ⇋ M) with different R_2 values for the major and minor states to obtain the $\Delta\varpi_{FM}$ values

temperatures implicitly assumes that the chemical shift differences between different states have a very weak temperature dependence.

Unique three-state solution from relative signs of $\Delta\varpi_{M1M2}$

The temperature dependencies of $\Delta\varpi_{FM1}$ values obtained from global two-state fits of ^{15}N CEST profiles ($B_1 \sim 20$ and ~ 50 Hz; Table S1) of the set11 residues from WT FF are plotted in Fig. 6. The $\Delta\varpi_{FM1}$ values for K26, I43, V67 and Q68 monotonically increase with temperature, while $\Delta\varpi_{FM1}$ of S56 monotonically decreases. Residues K26, I43, S56, Q68 and V67 for which the relative signs of $\Delta\varpi_{M1M2}$ are available will be referred to as the set5 residues, while the set6 class of residues consists of K41, S50, L52, A53, L55 and K59 for which relative signs are not available, as the two-state $\Delta\varpi_{FM1}$ values do not monotonically vary with temperature (Fig. 6). Based on the above discussion one possible constraint is that $\Delta\varpi_{M1M2}$ values for K26, I43, Q68 and V67 are all positive, while for S56 $\Delta\varpi_{M1M2} < 0$. A unique three-state solution ($p_{M1} = 0.36 \pm 0.01\%$, $p_{M2} = 0.15 \pm 0.01\%$, $k_{ex,FM1} = 1174 \pm 63$ s^{-1}, $k_{ex,FM2} = 533 \pm 158$ s^{-1}, $k_{ex,M1M2} = 4895 \pm 295$ s^{-1}; Fig. 7) with $\chi^2_{red} = 0.74$ emerges in this case when the ^{15}N CEST data from the set5 residues are analysed. This is illustrated in Fig. 7 where the results from 100 bootstrap trials obtained with the $\Delta\varpi_{M1M2}$ constraints are plotted in blue,

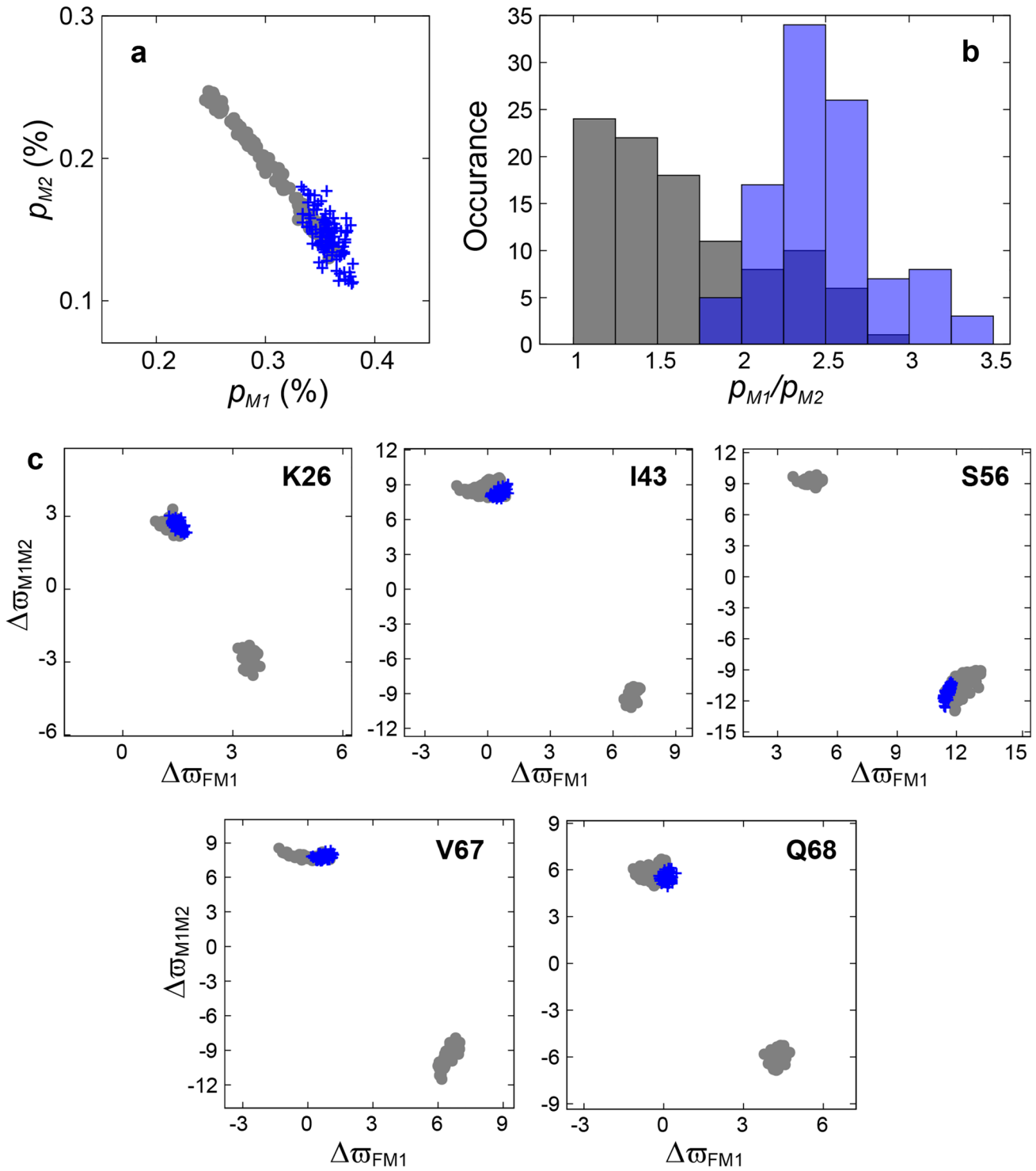

Fig. 7 Analysis of WT FF ^{15}N CEST data (15 °C) with constraints on the relative signs of $\Delta\varpi_{M1M2}$ values for five residues (K26, I43, S56, V67 and Q68) results in a well-defined three-state exchange model. **a** Plot showing the p_{M1} and p_{M2} values obtained from 100 bootstrap trials with (blue crosses) and without (grey circles) $\Delta\varpi_{M1M2}$ sign constraints. **b** Histogram showing the distribution of p_{M1}/p_{M2} values obtained from 100 bootstrap trials with (blue) and without (grey) $\Delta\varpi_{M1M2}$ sign constraints. **c** $\Delta\varpi_{FM1}$ and $\Delta\varpi_{M1M2}$ values (ppm) obtained from 100 bootstrap trials with (blue crosses) and without (grey circles) $\Delta\varpi_{M1M2}$ sign constraints. The best fit parameters (**a**, **c**) and the distribution (**b**) shown in grey are from Fig. 3, obtained by analysing ^{15}N CEST data from 11 residues without the $\Delta\varpi_{M1M2}$ sign constraints

while for comparison results from Fig. 3 obtained without knowledge of the signs of $\Delta\varpi_{M1M2}$ are shown in grey. It clear that there is far less correlation between p_{M1} and p_{M2} (Fig. 7a) and p_{M1}/p_{M2} is now better defined (1.85 to 3.4; Fig. 7b). Note that unlike the case in Fig. 3 where the condition $p_{M1} > p_{M2}$ was imposed to label states M1 and M2, there is no constraint on the relative magnitudes of the populations in the analysis when the signs of $\Delta\varpi_{M1M2}$ are constrained. Importantly, the twofold degeneracy in each $\Delta\varpi_{M1M2}$ and $\Delta\varpi_{FM1}$ pair that is noted when the signs of $\Delta\varpi_{M1M2}$ values are not available is lifted once the sign information is incorporated in the fits, as expected (Fig. 7c).

The analysis presented in Fig. 7a–c is based on the assumption that $\Delta\varpi_{M1M2}$ values for one group of residues are positive and the second group negative. In principle, the temperature dependent data of Fig. 6 only provides the relative signs of $\Delta\varpi_{M1M2}$ for each group. Therefore, we repeated the analysis as described above with the signs of $\Delta\varpi_{M1M2}$ in each group inverted. The same unique three-state solution was obtained with the exception that the labels M1 and M2 were interchanged (Figs. S1, S2). Thus, despite having two possible sets of consistent $\Delta\varpi_{M1M2}$ values, only one three-state solution emerges, and there is, therefore, no need to perform model selection from two separate fits. Analysis of χ^2_{red} surfaces suggests that inclusion of the signs of $\Delta\varpi_{M1M2}$ eliminates wrong spurious minima and smoothens the resulting surface so that the minimiser can find the global minimum (Fig. S2), without the need to resort to an extensive grid search. In the future we will also explore the utility of CEST experiments recorded with specific B_1 fields applied at particular offsets informed by theoretical results to obtain the $\Delta\varpi_{M1M2}$ sign information (Auer et al. 2009; Koss et al. 2023).

It is noteworthy that exchange parameters were only very poorly defined in studies of a number of different exchanging protein systems when single-quantum ^{15}N CPMG data recorded at a single temperature were analysed using a three-state model, with precise three-state exchange parameters obtained only by analysis of a combination of single and multiple-quantum CPMG data using an extensive grid-search over fitting parameter space to identify the global minimum in the χ^2_{red} surface (Korzhnev et al. 2005; Neudecker et al. 2006). Similarly, an analysis of single-quantum ^{15}N CPMG data recorded at multiple temperatures and analysed using a three-state model that assumes that the chemical shift differences between corresponding spins in different states are temperature independent only converged when an extensive grid search procedure was used (Korzhnev et al. 2004; Neudecker et al. 2006). It appears, therefore, that CEST experiments may be preferred over CPMG data in many cases for the robust analysis of three-state exchanging systems.

WT FF populates both I1 and I2 at 15 °C

Having a robustly defined set of exchange parameters we next sought to obtain the ϖ_{M1} and ϖ_{M2} values for the set6 residues (K41, S50, L52, A53, L55 and K59) for which the signs of $\Delta\varpi_{M1M2}$ were not available. Here we used a bootstrap procedure with 100 trials where in each trial the global three-state exchange parameters (p_{M1}, p_{M2}, $k_{ex,FM1}$, $k_{ex,FM2}$, $k_{ex,M1M2}$) were fixed to one of the realisations from the bootstrap analysis of the set5 residues (Fig. 7), while the residue specific parameters ($\Delta\varpi_{FM1}$, $\Delta\varpi_{FM2}$, and $R_{2,F}$) were fit. The 100 best-fit $\Delta\varpi_{FM1}$ and $\Delta\varpi_{M1M2}$ values for each residue are shown in Fig. 8. $\Delta\varpi_{FM1}$ and $\Delta\varpi_{M1M2}$ values are now well defined (blue crosses) for K41 and K59. In the case of S50 and A53 there is a ($\Delta\varpi_{FM1}$, $\Delta\varpi_{M1M2}$) pair that is preferred in greater than 75% of the cases (Fig. 8b) and greater than 90% of the cases when the analysis is performed on data recorded at 20 °C (Fig. S3). In what follows; therefore, we take the preferred shift pair for each of these residues to be the correct one. In the case of L52 there is a broad distribution of $\Delta\varpi_{M1M2}$ values around ~ 2 ppm, however, the second solution at an expected position of approximately − 2 ppm has been eliminated (Fig. 8b). $\Delta\varpi_{FM1}$ and $\Delta\varpi_{M1M2}$ are still poorly defined for L55 so that the minor state shifts cannot be established for this residue. Taken together, chemical shifts for M1 and M2 are available for 10 (set10) of the 11 residues that were analysed.

Analysis of the ^{15}N CEST profiles recorded at 15 °C using a two-state model of chemical exchange with variable transverse relaxation rates for corresponding spins in each state established that one of the interconverting conformations was the A39G FF I2 state (Fig. 2e). Not surprisingly, the CEST derived ^{15}N chemical shifts of residues in one of the WT FF minor states (M1 state) determined from the three-state analysis described above correspond to those of A39G FF I2 (RMSD 0.7 ppm; Fig. 9a); these shifts are distinct from those of the A39G FF I1 state (RMSD 4.6 ppm; Fig. 9b). Notably, the CEST derived chemical shifts of the second WT FF minor state (M2) are not similar to those of the A39G FF I2 state (RMSD 5.6 ppm; Fig. 9c) but, rather, are well correlated with the shifts of the A39G FF I1 state (RMSD 1.6 ppm; Fig. 9d). Thus, analysis of the ^{15}N CEST data clearly establishes that WT FF populates both I1 and I2 states on the millisecond timescale at 15 °C. The sensitivity of these ^{15}N CEST datasets to multiple states is made clear by the fact that the combined population of I1 and I2 at 15 °C is just ~ 0.5%.

The backbone ^{15}N $\Delta\varpi_{FI1}$ and $\Delta\varpi_{FI2}$ values for the WT FF domain, obtained from analysis of the CEST data recorded at 15 °C, are listed in Table S2. The very large $\Delta\varpi_{FI2}$ and $\Delta\varpi_{I1I2}$ values for S56 stand out and we wondered how critical the data from this residue are in defining the exchange parameters and the chemical shifts of the

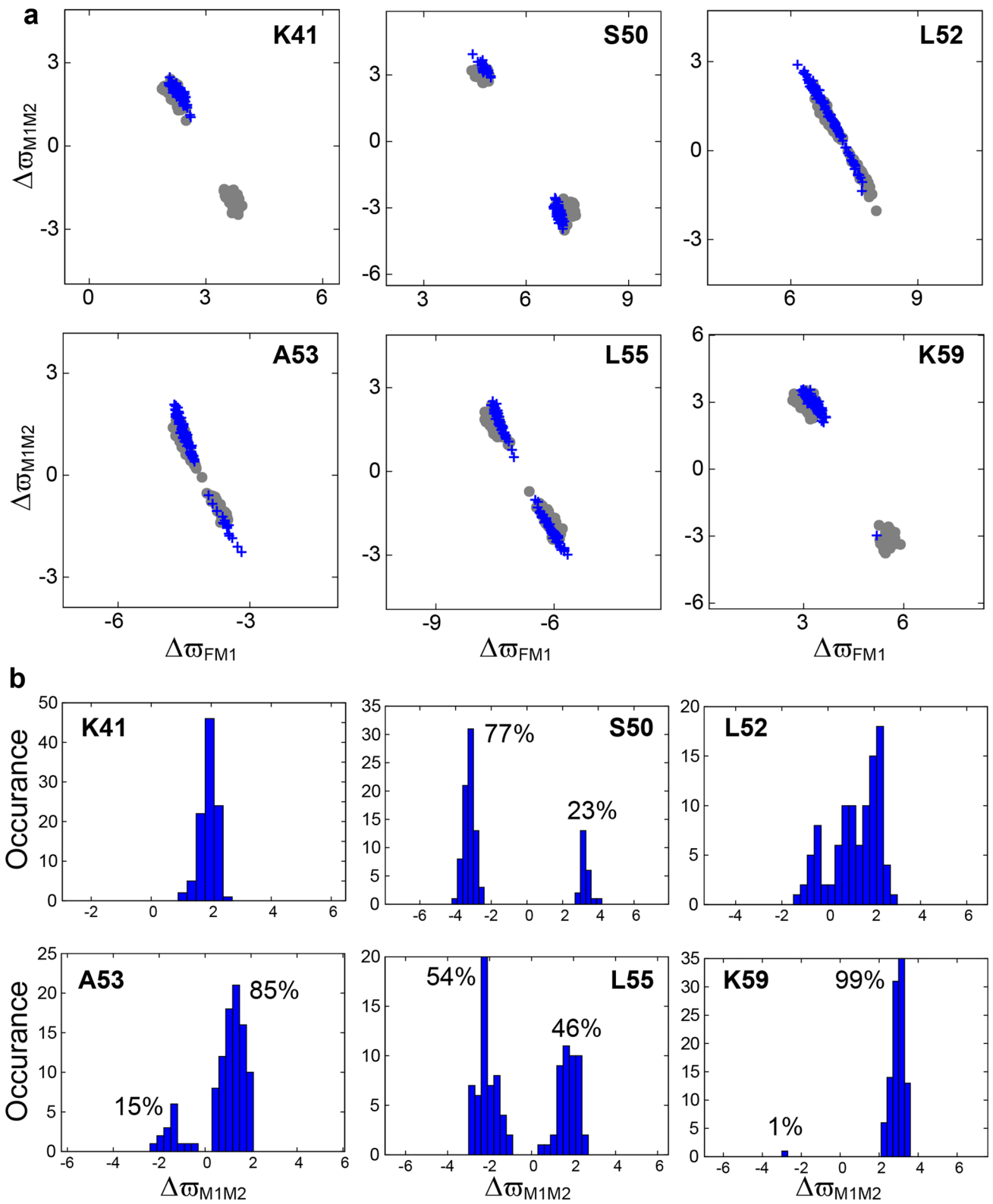

interconverting states. When the ^{15}N CEST data ($B_1 = 20.8$ and 52 Hz) from 10 residues (set11 excluding S56) were analysed using a two-state (F ⇌ M) model the quality of the fits improved ($\chi^2_{red} = 1.3$ to 0.7) when the constraint $R_{2,M} = R_{2,F}$ was removed showing that the data from S56 are not

◂**Fig. 8** Analysis of WT FF ^{15}N CEST data (15 °C) for residues with minor state dips showing little temperature dependence such that the relative signs of $\Delta\varpi_{M1M2}$ are not available. **a** $\Delta\varpi_{M1M2}$ vs. $\Delta\varpi_{FM1}$ plots for different sites from 100 bootstrap trials. The exchange parameters were fixed to those obtained from fits of profiles for K26, I43, S56, V67 and Q68 for which the relative signs of $\Delta\varpi_{M1M2}$ are available (see text and Fig. 7) and the resulting shift differences are shown in blue, superimposed on the distributions from Fig. 3 (in grey) where sign information was not available. **b** Distribution of $\Delta\varpi_{M1M2}$ values from the 100 bootstrap trials in **a**. Unique $\Delta\varpi_{M1M2}$, $\Delta\varpi_{FM1}$ solutions emerge for K41 and K59, while $\Delta\varpi_{M1M2}$, $\Delta\varpi_{FM1}$ values can also be extracted for S50, L52 and A53 (see text) but not for L55

needed to establish that WT FF populates at least two minor states at 15 °C. However, while performing a three-state analysis of the ^{15}N CEST data using only the four residues (other than S56) for which the relative signs of $\Delta\varpi_{I1I2}$ are available (Fig. 6) the populations, p_{M1} and p_{M2}, were less well defined (Fig. S4) and the exchange rates were substantially altered. However, qualitatively correct $\Delta\varpi_{FI1}$ and $\Delta\varpi_{FI2}$ values still result (Fig. S4). This is due to the fact that the width of the minor state dip provides insight into the relative shift differences of the corresponding spins in I1 and I2 in the case of rapid exchange between the states, with a broad (narrow) dip indicating large(small) $\Delta\varpi_{I1I2}$ shift differences. Thus, accurate shifts can be obtained even when exchange rates are not well defined. In this regard, CEST is preferred over CPMG where in the latter robust estimates of chemical shifts are predicated on fitting accurate exchange parameters. We have further investigated whether removal of other residues from set5 ({K26, I43, S56, Q68 and V67}), one at a time, would impact the extracted rates and populations as was the case for S56. Notably, however, the fitted parameters were robust, and the effects were small (Fig. S5; Table S3). The special importance of S56 and the results summarized in Table S3 are not surprising. The uniquely large $\Delta\varpi_{FI2}$ and $\Delta\varpi_{I1I2}$ values for S56 ensure that I1 and I2 are distinguishable despite the rapid I1/I2 exchange ($\left|\frac{k_{ex,I1I2}}{\Delta\omega_{I1I2}}\right| \sim 1$) and the large $\Delta\varpi_{FI2}$ enables $k_{ex,FI2}$ to be fit robustly. In the absence of S56, $k_{ex,FI2}$ is effectively not defined. In a similar manner, I43, V67, and Q68 are responsible for ensuring that an accurate value of $k_{ex,FI1}$ can be obtained. However, because of the redundancy removal of any one of these residues has only a relatively small influence on the extracted exchange parameters.

The I1 state cannot be detected from analysis of ^{15}N CPMG experiments recorded at 15 °C

Having established that both of the I1 and I2 minor states that had been observed previously in studies of A39G FF (Tiwari et al. 2021) could be detected through the analysis of ^{15}N CEST experiments recorded on WT FF we next asked whether analysis of the corresponding CPMG data could also provide an avenue for detection of the two folding intermediates. To this end synthetic ^{15}N CPMG relaxation dispersion profiles (B_0 fields of 11.7 and 18.8 T) were generated using the ^{15}N CEST derived three-state exchange model (Fig. 10a, b) for the 10 sites (set10) for which the ^{15}N CEST derived I1 and I2 chemical shifts are available at 15 °C. The sizes of the $R_{2,eff}$ dispersions [$R_{2,eff}$(50Hz)-$R_{2,eff}$(1000Hz)] in the synthetic ^{15}N CPMG data are small (< 5 s^{-1}) because the populations of the minor states are small (p_{M1}= 0.36%, p_{M2} = 0.15%). The data were well fit globally to a two-state exchange model with an exchange rate of 920 ± 128 s^{-1} and a minor state population of 0.47 ± 0.04% (χ^2_{red}= 1). The fitted two-state $\Delta\varpi$ values ($\Delta\varpi^{2ST}_{CPMG}$) are in good agreement (RMSD 1 ppm; Fig. 10c) with the ^{15}N CEST derived values of the M1 (I2) state but not with the corresponding shift differences from the M2 (I1) state (RMSD 5.2 ppm; Fig. 10d), indicating that the I1 state is invisible to CPMG data recorded at 15 °C. Notably, ^{15}N CPMG experiments (11.7 and 18.8 T) recorded on WT FF that were carried out between 20 and 35 °C (and analysed together assuming temperature invariant chemical shifts) were sensitive to I1 and not I2 (Korzhnev et al. 2007). Thus, unlike the ^{15}N CEST data for which there is a clear indication from two-state fits that additional conformers are present (Fig. 2), the ^{15}N CPMG data (Fig. 10a, b and in the work of Korzhnev et al. 2007) are well satisfied with a model involving only a single minor conformer. The distinction arises because the width of a minor state CEST dip is particularly sensitive to exchange processes involving extra conformers.

^{15}N CEST supports WT FF populating at least two minor states at 30 °C

The exchange parameters extracted from the CEST data recorded at 15 °C ranged from $k_{ex,FM2}$ ~ 500 s^{-1} to $k_{ex,M1M2}$ ~ 5000 s^{-1}. We wondered whether systems with higher rates could also be analysed to produce robust models of exchange, and specifically in the present case whether both I1 and I2 could still be detected. To this end we recorded ^{15}N CEST data of WT FF at 30 °C using B_1 values of 21, 52.3, 104.6 and 209.3 Hz. As with the profiles recorded at the lower temperature, the data are incompatible with a simple two-state exchange model (χ^2_{red}= 2.2; Fig. 11a) where the major and minor states have the same R_2 values. Analysis of the data using a three-state exchange model in which the F state and the minor states M1 and M2 exchange with each other resulted in reasonably good fits (χ^2_{red}= 1.3; Fig. 11b). However, in contrast to the analysis of the 15 °C data, p_{M1} and p_{M2} could not be defined despite imposing constraints on the signs of $\Delta\varpi_{M1M2}$ (purple circles Fig. 11c) presumably

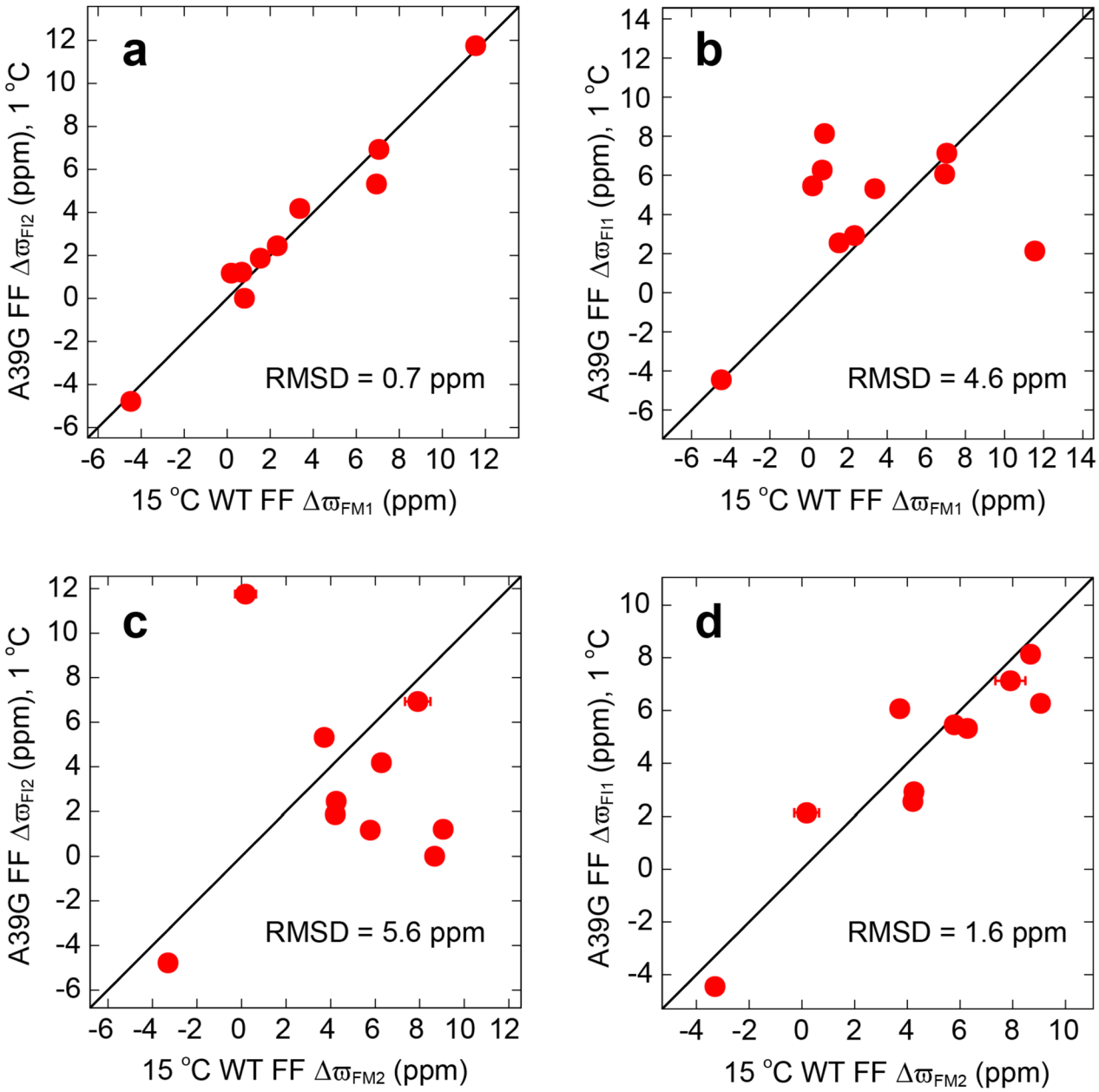

Fig. 9 $\Delta\varpi$ values from analysis of ^{15}N CEST data establish that WT FF populates two folding intermediates, I1 and I2, at 15 °C. Comparison of the CEST derived $\Delta\varpi_{FM1}$ values of WT FF with the A39G FF $\Delta\varpi_{FI2}$ (**a**) and A39G FF $\Delta\varpi_{FI1}$ (**b**) values. Comparison of the CEST derived $\Delta\varpi_{FM2}$ values of WT FF with the A39G FF $\Delta\varpi_{FI2}$ (**c**) and A39G FF $\Delta\varpi_{FI1}$ (**d**) values. A39G FF $\Delta\varpi_{FI1}$ and $\Delta\varpi_{FI2}$ values were obtained previously by fitting a four-state model to ^{15}N CEST data recorded at 1 °C (Tiwari et al. 2021)

because M1 and M2 are in very rapid exchange. Next, we analysed the ^{15}N CEST data as before but with $\Delta\varpi_{FM1}$ and $\Delta\varpi_{FM2}$ constrained to be within 1 ppm of the values obtained at 15 °C (Table S2). More precise best-fit exchange parameters were now obtained ($p_{M1} = 0.96 \pm 0.05\%$, $p_{M2} = 0.83 \pm 0.05\%$, $k_{ex,FM1} = 3567 \pm 167$ s^{-1}, $k_{ex,FM2} = 946 \pm 208$ s^{-1}, $k_{ex,M1M2} = 18{,}444 \pm 1543$ s^{-1}; compare purple and green circles in Fig. 11c) without degrading the quality of the fits ($\chi^2_{red} = 1.3$).

Finally, we generated ^{15}N CPMG data ($B_0 = 11.7$ and 18.8 T; Fig. 12a, b) using the three-state model parameters obtained above. The simulated ^{15}N CPMG data could be well fit using a two-state exchange model with an exchange rate of 2263 ± 55 s^{-1} and a minor state population of $1.7 \pm 0.02\%$ ($\chi^2_{red} = 1.1$), with the fitted $\Delta\varpi^{2ST}_{CPMG}$ values in good agreement with $\Delta\varpi_{FI1}$ previously obtained (RMSD 0.4 ppm; Fig. 12c) using CPMG experiments (Korzhnev et al. 2007). Thus, the analysis of the ^{15}N CEST data carried

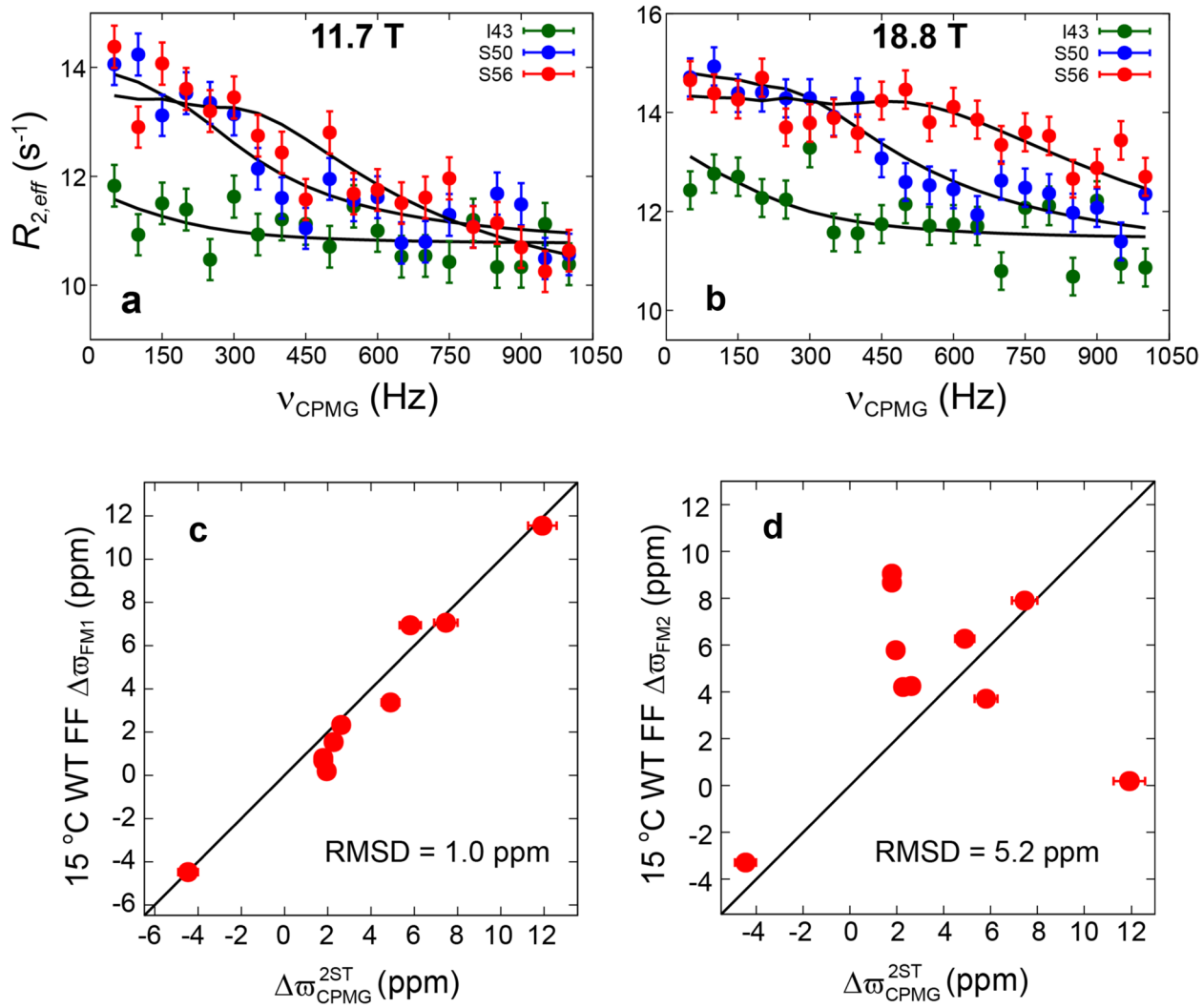

Fig. 10 The I1 state for WT FF at 15 °C as observed through ^{15}N CEST cannot be detected through ^{15}N CPMG experiments. ^{15}N CPMG data were generated (see "Materials and methods" section) for static field strengths of 11.7 and 18.8 T using CEST derived three-state exchange parameters based on analysis of ten residues (see text; set10). A two-state model with an exchange rate of 920 ± 128 s^{-1} and minor state population of 0.47 ± 0.04% satisfies (χ^2_{red} = 1) the synthetic CPMG data. In **a** and **b**, the circles are simulated CPMG data while the black line is drawn using the best fit two-state exchange parameters. Comparison of $\Delta\varpi$ values obtained by fitting a two-state model ($\Delta\varpi^{2ST}_{CPMG}$) to the synthetic three-state CPMG data with the ^{15}N CEST derived WT FF $\Delta\varpi_{FM1}$ (**c**) and $\Delta\varpi_{FM2}$ (**d**) values. Signs of $\Delta\varpi^{2ST}_{CPMG}$ were set to those of ^{15}N CEST derived two-state $\Delta\varpi_{FM}$ values (Fig. 2e)

out here clearly shows that the WT FF populates two minor states at 30 °C, corresponding to the folding intermediates I1 and I2. It is also the case that the rapid interconversion rates at 30 °C ($k_{ex,M1M2}$ ~ 18,000 s^{-1}) preclude a robust analysis of exchange parameters that was possible at 15 °C ($k_{ex,M1M2}$ ~ 5000 s^{-1}).

Concluding remarks

Here we have explored the utility of ^{15}N CEST experiments to characterise conformational exchange between three distinct states of WT FF, where the two minor conformers are populated at levels of 0.35% and 0.15% and where the exchange between them is on the order of 5000 s^{-1}. Under these conditions only a single minor state dip is observed in CEST profiles, yet fits of the data to a two-state interconversion model clearly establish that an additional conformer is present. Using the linewidth of the minor dip and its temperature dependence it is possible to map the energy landscape and to obtain chemical shifts of all three interconverting states from analysis of ^{15}N CEST data recorded at a single temperature rather than an involved (simultaneous) analysis of data recorded at multiple temperatures. Notably, complex and time-consuming grid searches over parameter space that have previously been used in the

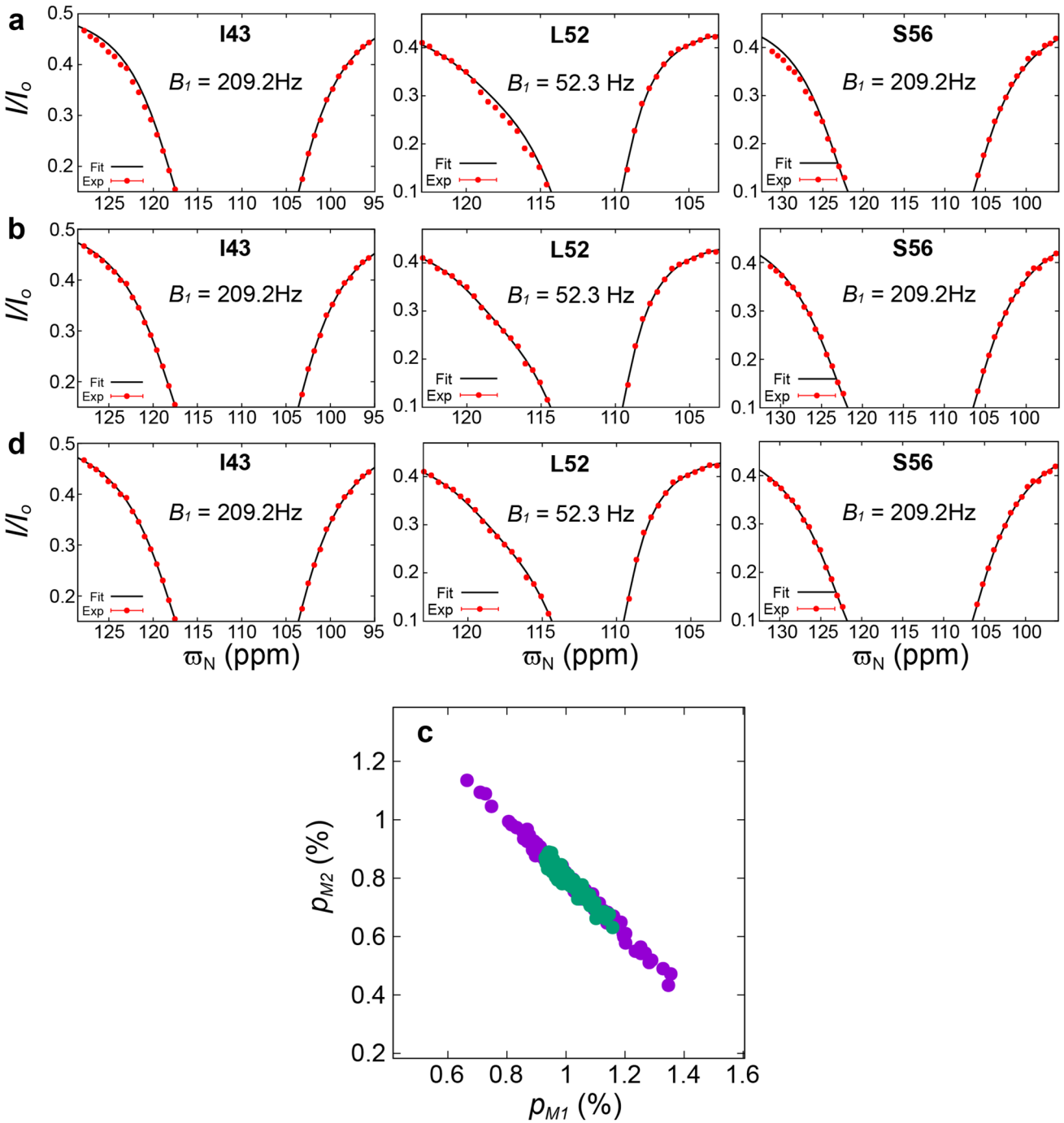

Fig. 11 ^{15}N CEST data recorded at 30 °C can only be explained on the basis of WT FF populating at least a pair of minor states. **a** WT FF ^{15}N CEST data recorded at 30 °C is not well fit by a two-state exchange model with equal transverse relaxation rates in the interconverting states (χ^2_{red}= 2.2), but is reasonably well-satisfied by a three-state exchange model (χ^2_{red}= 1.3) using $\Delta\varpi_{M1M2}$ sign constraints, where F exchanges with minor states M1 and M2 (**b**). **c** Best fit p_{M1} and p_{M2} values obtained from 100 bootstrap trials with constraints on the signs of $\Delta\varpi_{M1M2}$ (purple circles) or by constraining $\Delta\varpi_{FM1}$ and $\Delta\varpi_{FM2}$ to within 1 ppm of the values obtained at 15 °C (green circles). Addition of the $\Delta\varpi_{FM1}$ and $\Delta\varpi_{FM2}$ constraints (**d**) did not affect the quality of fits (χ^2_{red}= 1.3) but resulted in better defined p_{M1} and p_{M2} values (compare purple and green circles in **c**)

analysis of multi-site exchange using CPMG experiments were not required because the relative signs of $\Delta\varpi_{M1M2}$ that are obtained by analysing the ^{15}N CEST data recorded at different temperatures removes the two-fold ambiguity in each $\Delta\varpi_{M1M2}$ value, simplifying the χ^2_{red} surface so that the global minimum can be achieved.

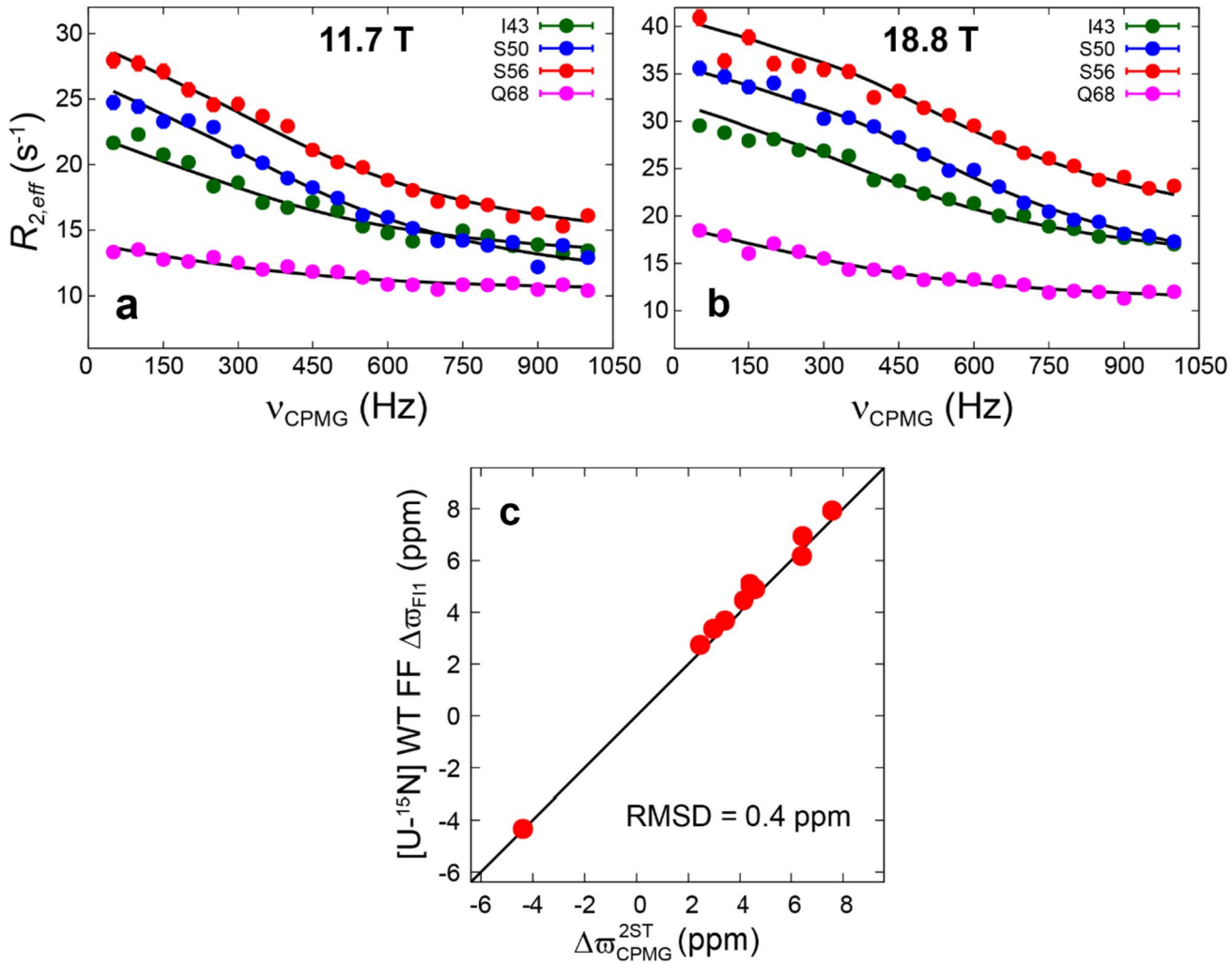

Fig. 12 Synthetic ^{15}N CPMG data generated using a three-state model of exchange along with parameters based on fits of 30 °C ^{15}N CEST data are well-fit to a two-site interconversion process. ^{15}N CPMG data were generated using static magnetic fields of 11.7 (**a**) and 18.8 T (**b**) with CEST derived three-state exchange parameters obtained from fits of profiles for a set of ten residues (set10) recorded at 30 °C. A two-state model (exchange rate: 2263 ± 55 s^{-1}, minor state population: 1.7 ± 0.02%) fits the synthetic CPMG data well (χ^2_{red} = 1.1), indicating that the CPMG experiment is not sensitive to the extra minor state that is observed through analysis of CEST data. Simulated CPMG data is represented using circles in **a** and **b** while the black line is based on the best-fit two-state exchange parameters. Comparison of the $\Delta\varpi$ values ($\Delta\varpi^{2ST}_{CPMG}$) obtained by fitting a two-state model to the synthetic three-state CPMG data with $\Delta\varpi_{FI1}$ values derived from ^{15}N CPMG data recorded on a [U-^{15}N] WT FF sample (Korzhnev et al. 2007) over a 20–35 °C temperature range. Signs for all the $\Delta\varpi$ values are from Korzhnev et al. (2010)

Traditionally CPMG experiments have been used to study systems with exchange rates between states on the order of many hundreds/second or greater, while CEST analyses have focused on molecules that exchange between conformers with rates less than a few hundred per second. The present study clearly indicates that CEST can be useful to explore faster processes and that, at least in some cases, there may be distinct advantages over CPMG. For example, in the case of WT FF where ^{15}N CEST data clearly indicates an exchange process between more than two states at 15 °C, the corresponding ^{15}N CPMG data were consistent with a two-state interconversion. In addition, extraction of robust parameters for exchanging systems involving conformers with different transverse relaxation rates is more readily achieved with CEST data because linewidths are available simply by inspection, while CPMG-based profiles do not report directly on the minor state linewidths (Hansen et al. 2009) and consequently are often analysed, sometimes erroneously, by assuming that corresponding spins in different conformers have equivalent relaxation times. Finally, the long T_{EX} delays that can be used to measure exchange where relaxation of the signal of interest is governed by R_1, rather than R_2 as for CPMG, increases the range of CEST experiments to studies of exchanging systems with lower

populations (as low as 0.1%; Ramanujam et al. 2019; Rangadurai et al. 2019; Tiwari et al. 2021) than typically explored through CPMG measurements. It is likely that the utility of CEST-based applications will continue to increase, adding to the NMR tool-kit for studies of biomolecular conformational exchange.

Supplementary Information The online version contains supplementary material available at https://doi.org/10.1007/s10858-023-00431-6.

Acknowledgements We thank Dr. G. Bouvignies (Ecole Normale Superieure, Paris) for providing the program *ChemEx*, the TIFR-Hyderabad NMR Facility for access to the NMR facilities, and Dr. K. Rao for maintenance of the facility. PV acknowledges intramural funding from TIFR Hyderabad (DAE, Government of India, Project No. RTI 4007). Support to LEK was provided from the Canadian Institutes of Health Research (FND-503573) and the Natural Sciences and Engineering Council of Canada (2015-04347).

Author contributions All authors reviewed the manuscript.

Declarations

Conflict of interest The authors declare no competing interests.

References

Ahlner A, Carlsson M, Jonsson BH, Lundstrom P (2013) PINT: a software for integration of peak volumes and extraction of relaxation rates. J Biomol NMR 56:191–202

Allen M, Friedler A, Schon O, Bycroft M (2002) The structure of an FF domain from human HYPA/FBP11. J Mol Biol 323:411–416

Allerhand A, Thiele E (1966) Analysis of Carr-Purcell spin-echo NMR experiments on multiple-spin systems. II. The effect of chemical exchange. J Chem Phys 45:902–916

Anthis NJ, Clore GM (2015) Visualizing transient dark states by NMR spectroscopy. Q Rev Biophys 48:35–116

Auer R, Neudecker P, Muhandiram DR, Lundstrom P, Hansen DF, Konrat R, Kay LE (2009) Measuring the signs of 1H(alpha) chemical shift differences between ground and excited protein states by off-resonance spin-lock R(1rho) NMR spectroscopy. J Am Chem Soc 131:10832–10833

Bahar I, Jernigan R, Dill KA (2017) Protein actions: principles and modeling. Garland Science, Taylor & Francis Group, New York

Bezsonova I, Korzhnev DM, Prosser RS, Forman-Kay JD, Kay LE (2006) Hydration and packing along the folding pathway of SH3 domains by pressure-dependent NMR. Biochemistry 45:4711–4719

Bouvignies G (2011) ChemEx. https://github.com/gbouvignies/chemex

Bouvignies G, Kay LE (2012) A 2D $^{(1)(3)}$C-CEST experiment for studying slowly exchanging protein systems using methyl probes: an application to protein folding. J Biomol NMR 53:303–310

Bouvignies G, Vallurupalli P, Hansen DF, Correia BE, Lange O, Bah A, Vernon RM, Dahlquist FW, Baker D, Kay LE (2011) Solution structure of a minor and transiently formed state of a T4 lysozyme mutant. Nature 477:111–114

Bouvignies G, Vallurupalli P, Kay LE (2014) Visualizing side chains of invisible protein conformers by solution NMR. J Mol Biol 426:763–774

Cabrera Allpas R, Hansen AL, Bruschweiler R (2023) ARCHENOAH: NMR supersequence with five different CEST experiments for studying protein conformational dynamics. Phys Chem Chem Phys 25:16217–16221

Carr HY, Purcell EM (1954) Effects of diffusion on free precession in nuclear magnetic resonance experiments. Phys Rev 94:630–638

Cavanagh J, Fairbrother WJ, Palmer AG, Rance M, Skelton NJ (2006) Protein NMR spectroscopy, principles and practice, 2nd edn. Academic, New York

Choy WY, Zhou Z, Bai Y, Kay LE (2005) An 15N NMR spin relaxation dispersion study of the folding of a pair of engineered mutants of apocytochrome b562. J Am Chem Soc 127:5066–5072

Chung HS, Piana-Agostinetti S, Shaw DE, Eaton WA (2015) Structural origin of slow diffusion in protein folding. Science 349:1504–1510

Delaglio F, Grzesiek S, Vuister GW, Zhu G, Pfeifer J, Bax A (1995) NMRPipe—a multidimensional spectral processing system based on Unix pipes. J Biomol NMR 6:277–293

Deverell C, Morgan RE, Strange JH (1970) Studies of chemical exchange by nuclear magnetic relaxation in rotating frame. Mol Phys 18:553

Fawzi NL, Ying JF, Torchia DA, Clore GM (2010) Kinetics of amyloid beta monomer-to-oligomer exchange by NMR relaxation. J Am Chem Soc 132:9948–9951

Fawzi NL, Ying J, Ghirlando R, Torchia DA, Clore GM (2011) Atomic-resolution dynamics on the surface of amyloid-beta protofibrils probed by solution NMR. Nature 480:268–272

Forsen S, Hoffman RA (1963) Study of moderately rapid chemical exchange reactions by means of nuclear magnetic double resonance. J Chem Phys 39:2892–2901

Frauenfelder H, Sligar SG, Wolynes PG (1991) The energy landscapes and motions of proteins. Science 254:1598–1603

Goddard TD, Kneller DG (2008) SPARKY 3. University of California, San Francisco

Gopalan AB, Vallurupalli P (2018) Measuring the signs of the methyl ^{1}H chemical shift differences between major and 'invisible' minor protein conformational states using methyl ^{1}H multi-quantum spectroscopy. J Biomol NMR 70:187–202

Gopalan AB, Hansen DF, Vallurupalli P (2018a) CPMG experiments for protein minor conformer structure determination. Methods Mol Biol 1688:223–242

Gopalan AB, Yuwen T, Kay LE, Vallurupalli P (2018b) A methyl $^{(1)}$H double quantum CPMG experiment to study protein conformational exchange. J Biomol NMR 72:79–91

Grey MJ, Wang C, Palmer AG 3rd (2003) Disulfide bond isomerization in basic pancreatic trypsin inhibitor: multisite chemical exchange quantified by CPMG relaxation dispersion and chemical shift modeling. J Am Chem Soc 125:14324–14335

Guenneugues M, Berthault P, Desvaux H (1999) A method for determining B_1 field inhomogeneity. Are the biases assumed in heteronuclear relaxation experiments usually underestimated? J Magn Reson 136:118–126

Hansen AL, Kay LE (2014) Measurement of histidine pK_a values and tautomer populations in invisible protein states. Proc Natl Acad Sci USA 111:E1705–E1712

Hansen DF, Vallurupalli P, Kay LE (2008) An improved ^{15}N relaxation dispersion experiment for the measurement of millisecond time-scale dynamics in proteins. J Phys Chem B 112:5898–5904

Hansen DF, Vallurupalli P, Kay LE (2009) Measurement of methyl group motional parameters of invisible, excited protein states by NMR spectroscopy. J Am Chem Soc 131:12745–12754

Jemth P, Gianni S, Day R, Li B, Johnson CM, Daggett V, Fersht AR (2004) Demonstration of a low-energy on-pathway intermediate in a fast-folding protein by kinetics, protein engineering, and simulation. Proc Natl Acad Sci USA 101:6450–6455

Jemth P, Johnson CM, Gianni S, Fersht AR (2008) Demonstration by burst-phase analysis of a robust folding intermediate in the FF domain. Protein Eng Des Sel 21:207–214

Karplus M, Kuriyan J (2005) Molecular dynamics and protein function. Proc Natl Acad Sci USA 102:6679–6685

Karunanithy G, Reinstein J, Hansen DF (2020) Multiquantum chemical exchange saturation transfer NMR to quantify symmetrical exchange: application to rotational dynamics of the guanidinium group in arginine side chains. J Phys Chem Lett 11:5649–5654

Khandave NP, Sekhar A, Vallurupalli P (2023) Studying micro to millisecond protein dynamics using simple amide $^{(15)}$N CEST experiments supplemented with major-state R(2) and visible peak-position constraints. J Biomol NMR 77(4):165–181

Korzhnev DM, Salvatella X, Vendruscolo M, Di Nardo AA, Davidson AR, Dobson CM, Kay LE (2004) Low-populated folding intermediates of Fyn SH3 characterized by relaxation dispersion NMR. Nature 430:586–590

Korzhnev DM, Neudecker P, Mittermaier A, Orekhov VY, Kay LE (2005) Multiple-site exchange in proteins studied with a suite of six NMR relaxation dispersion experiments: an application to the folding of a Fyn SH3 domain mutant. J Am Chem Soc 127:15602–15611

Korzhnev DM, Religa TL, Lundstrom P, Fersht AR, Kay LE (2007) The folding pathway of an FF domain: characterization of an on-pathway intermediate state under folding conditions by $^{(15)}$N, $^{(13)}$C(alpha) and $^{(13)}$C-methyl relaxation dispersion and $^{(1)}$H/$^{(2)}$H-exchange NMR spectroscopy. J Mol Biol 372:497–512

Korzhnev DM, Religa TL, Banachewicz W, Fersht AR, Kay LE (2010) A transient and low-populated protein-folding intermediate at atomic resolution. Science 329:1312–1316

Koss H, Rance M, Palmer AG (2017) General expressions for R1rho relaxation for N-site chemical exchange and the special case of linear chains. J Magn Reson 274:36–45

Koss H, Crawley T, Palmer AG III (2023) Site-based description of R(1)(rho) relaxation in local reference frames. J Magn Reson 347:107366

Kukic P, Pustovalova Y, Camilloni C, Gianni S, Korzhnev DM, Vendruscolo M (2017) Structural characterization of the early events in the nucleation-condensation mechanism in a protein folding process. J Am Chem Soc 139:6899–6910

Lee W, Tonelli M, Markley JL (2015) NMRFAM-SPARKY: enhanced software for biomolecular NMR spectroscopy. Bioinformatics 31:1325–1327

Levitt MH (1982) Symmetrical composite pulse sequences for NMR population-inversion. 2. Compensation of resonance offset. J Magn Reson 50:95–110

Lim J, Xiao TS, Fan JS, Yang DW (2014) An off-pathway folding intermediate of an acyl carrier protein domain coexists with the folded and unfolded states under native conditions. Angew Chem Int Ed Engl 53:2358–2361

Madhurima K, Nandi B, Munshi S, Naganathan AN, Sekhar A (2023) Functional regulation of an intrinsically disordered protein via a conformationally excited state. Sci Adv 9:eadh4591

Massi F, Grey MJ, Palmer AG 3rd (2005) Microsecond timescale backbone conformational dynamics in ubiquitin studied with NMR R1rho relaxation experiments. Protein Sci 14:735–742

McConnell HM (1958) Reaction rates by nuclear magnetic resonance. J Chem Phys 28:430–431

Meiboom S, Gill D (1958) Modified spin-echo method for measuring nuclear relaxation times. Rev Sci Instrum 29:688–691

Neudecker P, Korzhnev DM, Kay LE (2006) Assessment of the effects of increased relaxation dispersion data on the extraction of 3-site exchange parameters characterizing the unfolding of an SH3 domain. J Biomol NMR 34:129–135

Neudecker P, Robustelli P, Cavalli A, Walsh P, Lundstrom P, Zarrine-Afsar A, Sharpe S, Vendruscolo M, Kay LE (2012) Structure of an intermediate state in protein folding and aggregation. Science 336:362–366

Nielsen JT, Mulder FAA (2018) POTENCI: prediction of temperature, neighbor and pH-corrected chemical shifts for intrinsically disordered proteins. J Biomol NMR 70:141–165

Overbeck JH, Vogele J, Nussbaumer F, Duchardt-Ferner E, Kreutz C, Wohnert J, Sprangers R (2023) Multi-site conformational exchange in the synthetic neomycin-sensing riboswitch studied by $^{(19)}$F NMR. Angew Chem Int Ed Engl 62:e202218064

Palmer AG (2004) NMR characterization of the dynamics of biomacromolecules. Chem Rev 104:3623–3640

Palmer AG 3rd, Koss H (2019) Chemical exchange. Methods Enzymol 615:177–236

Palmer AG 3rd, Kroenke CD, Loria JP (2001) Nuclear magnetic resonance methods for quantifying microsecond-to-millisecond motions in biological macromolecules. Methods Enzymol 339:204–238

Press WH, Flannery BP, Teukolsky SA, Vetterling WT (1992) Numerical recipes in C. In: The art of scientific computing, 2nd edn. Cambridge University Press, Cambridge

Pritchard RB, Hansen DF (2019) Characterising side chains in large proteins by protonless $^{(13)}$C-detected NMR spectroscopy. Nat Commun 10:1747

Ramanujam V, Charlier C, Bax A (2019) Observation and kinetic characterization of transient Schiff base intermediates by CEST NMR spectroscopy. Angew Chem Int Ed Engl 58:15309–15312

Rangadurai A, Szymaski ES, Kimsey IJ, Shi H, Al-Hashimi H (2019) Characterizing micro-to-millisecond chemical exchange in nucleic acids using off-resonance R1ρ relaxation dispersion. Prog Nucl Magn Reson Spectrosc 112–113:55–102

Rangadurai A, Shi H, Al-Hashimi HM (2020) Extending the sensitivity of CEST NMR spectroscopy to micro-to-millisecond dynamics in nucleic acids using high-power radio-frequency fields. Angew Chem Int Ed Engl 59:11262–11266

Reddy JG, Pratihar S, Ban D, Frischkorn S, Becker S, Griesinger C, Lee D (2018) Simultaneous determination of fast and slow dynamics in molecules using extreme CPMG relaxation dispersion experiments. J Biomol NMR 70:1–9

Sanchez-Medina C, Sekhar A, Vallurupalli P, Cerminara M, Munoz V, Kay LE (2014) Probing the free energy landscape of the fast-folding gpW protein by relaxation dispersion NMR. J Am Chem Soc 136:7444–7451

Sekhar A, Kay LE (2013) NMR paves the way for atomic level descriptions of sparsely populated, transiently formed biomolecular conformers. Proc Natl Acad Sci USA 110:12867–12874

Sekhar A, Kay LE (2019) An NMR view of protein dynamics in health and disease. Annu Rev Biophys 48:297–319

Sekhar A, Latham MP, Vallurupalli P, Kay LE (2014) Viscosity-dependent kinetics of protein conformational exchange: microviscosity effects and the need for a small viscogen. J Phys Chem B 118:4546–4551

Skrynnikov NR, Dahlquist FW, Kay LE (2002) Reconstructing NMR spectra of "invisible" excited protein states using HSQC and HMQC experiments. J Am Chem Soc 124:12352–12360

Sugase K, Dyson HJ, Wright PE (2007) Mechanism of coupled folding and binding of an intrinsically disordered protein. Nature 447:1021–1025

Tiwari VP, Vallurupalli P (2020) A CEST NMR experiment to obtain glycine $^{(1)}$H(alpha) chemical shifts in 'invisible' minor states of proteins. J Biomol NMR 74:443–455

Tiwari VP, Toyama Y, De D, Kay LE, Vallurupalli P (2021) The A39G FF domain folds on a volcano-shaped free energy surface via separate pathways. Proc Natl Acad Sci USA 118(46):e2115113118

Trott O, Palmer AG 3rd (2004) Theoretical study of R(1rho) rotating-frame and R2 free-precession relaxation in the presence of n-site chemical exchange. J Magn Reson 170:104–112

Tugarinov V, Clore GM (2019) Exchange saturation transfer and associated NMR techniques for studies of protein interactions involving high-molecular-weight systems. J Biomol NMR 73:461–469

Vallurupalli P, Kay LE (2013) Probing slow chemical exchange at carbonyl sites in proteins by chemical exchange saturation transfer NMR spectroscopy. Angew Chem Int Ed Engl 52:4156–4159

Vallurupalli P, Hansen DF, Lundstrom P, Kay LE (2009) CPMG relaxation dispersion NMR experiments measuring glycine ^{1}H alpha and ^{13}C alpha chemical shifts in the 'invisible' excited states of proteins. J Biomol NMR 45:45–55

Vallurupalli P, Bouvignies G, Kay LE (2011) Increasing the exchange time-scale that can be probed by CPMG relaxation dispersion NMR. J Phys Chem B 115:14891–14900

Vallurupalli P, Bouvignies G, Kay LE (2012) Studying "invisible" excited protein States in slow exchange with a major state conformation. J Am Chem Soc 134:8148–8161

Vallurupalli P, Chakrabarti N, Pomes R, Kay LE (2016) Atomistic picture of conformational exchange in a T4 lysozyme cavity mutant: an experiment-guided molecular dynamics study. Chem Sci 7:3602–3613

Vallurupalli P, Sekhar A, Yuwen T, Kay LE (2017) Probing conformational dynamics in biomolecules via chemical exchange saturation transfer: a primer. J Biomol NMR 67:243–271

Vallurupalli P, Tiwari VP, Ghosh S (2019) A double-resonance CEST experiment to study multistate protein conformational exchange: an application to protein folding. J Phys Chem Lett 10:3051–3056

van Zijl PCM, Yadav NN (2011) Chemical exchange saturation transfer (CEST): what is in a name and what isn't? Magn Reson Med 65:927–948

Ward KM, Aletras AH, Balaban RS (2000) A new class of contrast agents for MRI based on proton chemical exchange dependent saturation transfer (CEST). J Magn Reson 143:79–87

Yuwen T, Sekhar A, Kay LE (2017) Separating dipolar and chemical exchange magnetization transfer processes in ^{1}H-CEST. Angew Chem Int Ed Engl 56:6122–6125

Yuwen T, Bah A, Brady JP, Ferrage F, Bouvignies G, Kay LE (2018a) Measuring solvent hydrogen exchange rates by multifrequency excitation $^{(15)}$N CEST: application to protein phase separation. J Phys Chem B 122:11206–11217

Yuwen T, Kay LE, Bouvignies G (2018b) Dramatic decrease in CEST measurement times using multi-site excitation. ChemPhysChem 19:1707–1710

Zhuravleva A, Korzhnev DM (2017) Protein folding by NMR. Prog Nucl Magn Reson Spectrosc 100:52–77